Numerical modelling of permafrost spring discharge and open-system pingo formation induced by basal permafrost aggradation

Mikkel T. Hornum[1,2], Andrew J. Hodson[1,3], Søren Jessen[2], Victor Bense[4], Kim Senger[1]

[1]Department of Arctic Geology, The University Centre in Svalbard (UNIS), N-9171 Longyearbyen, Norway.
5 [2]Department of Geosciences and Natural Resource Management, University of Copenhagen, 1350 Copenhagen K, Denmark.
[3]Department of Environmental Science, Western Norway University of Applied Sciences, N-6856 Sogndal, Norway
[4]Department of Environmental Sciences, Wageningen University, 6708PB Wageningen, Netherlands.

Correspondence to: Mikkel T. Hornum (mth@ign.ku.dk)

Abstract

10 In the high Arctic valley of Adventdalen, Svalbard, sub-permafrost groundwater feeds several pingo springs distributed along the valley axis. The driving mechanism for groundwater discharge and associated pingo formation is enigmatic because wet-based glaciers in the adjacent highlands and the presence of continuous permafrost seem to preclude recharge of the sub-permafrost groundwater system by either a sub-glacial source or a precipitation surplus. Since the pingo springs enable methane that has accumulated underneath the permafrost to escape directly to the atmosphere, our limited understanding of the

15 groundwater system brings significant uncertainty to the understanding of how methane emissions will respond to changing climate. We address this problem with a new conceptual model for open-system pingo formation wherein pingo growth is sustained by sub-permafrost pressure effects during millennial scale basal permafrost aggradation. We test the viability of this mechanism for generating groundwater flow with decoupled heat (1D-transient) and groundwater (2D-steady-state) transport modelling experiments. Our results show that the pingos in lower Adventdalen easily conform to this conceptual model.

20 Simulations suggest that the generally low-permeability hydrogeological units cause groundwater residence times that exceed the duration of the Holocene. The likelihood of such pre-Holocene groundwater ages is also supported by the hydrogeochemistry of the pingo springs, which demonstrate a sea-wards freshening of groundwater, potentially supplied by paleo-subglacial melting during the Weichselian. Such waters form a sub-permafrost fresh water wedge that progressively thins inland, where the duration of permafrost aggradation is longest. The mixing ratio of the underlying marine waters

25 therefore increases in this direction because less unfrozen freshwater is available for mixing. Although this unusual hydraulic system is most likely governed by permafrost aggradation, the potential for additional pressurisation is also explored. We conclude that methane production and methane clathrate formation may also affect hydraulic the pressure in sub-permafrost aquifers, but additional research is needed to fully establish their influence.

1   Introduction

30 Sub-permafrost groundwater systems are highly inaccessible and so their investigation usually relies on sparse data (van der Ploeg et al., 2012). However, cold regions increasingly become hydrogeologically active after surface warming and associated permafrost degradation. This implies, for example, an increased outflow of deeper groundwater to rivers and lakes (Bense et al., 2012), increased rates of biogeochemical processes (Grosse et al., 2016), and potentially increased fluxes of methane or other compounds into the surface environment and atmosphere (Schuster et al., 2018). The surface discharge of sub-permafrost

35 groundwater is currently exemplified by springs in the high Arctic (Andersen et al., 2002; Grasby et al., 2012; Haldorsen et al., 1996; Williams, 1970). If conditions are favorable, spring outflow may instead freeze below the active layer and initiate the growth of an ice-cored hill or pingo. By definition, this would classify as an open-system pingo because of the open connection to the sub-permafrost groundwater (Liestøl, 1996). Considerable methane stocks may exist below continuous permafrost and where no such springs exist, the only rapid escape route goes to the ocean, where methane oxidation prevents

40 much of it from reaching the atmosphere (Mau et al., 2017; Myhre et al., 2016). Where they do exist, however, sub-permafrost methane may escape directly to the atmosphere, contributing significantly to the total landscape methane emissions (Betlem et al., 2019; Hodson et al., In Review).

The hydrogeological mechanisms causing the sustained flow of sub-permafrost groundwater to surface springs remain elusive (Scheidegger et al., 2012). Earlier it was proposed that subglacial meltwater from underneath warm-based ice sheets

45 or glaciers would sufficiently recharge a sub-permafrost aquifer (Demidov et al., 2019; Liestøl, 1977; Scheidegger et al., 2012; Scheidegger and Bense, 2014). However, in regions of continuous permafrost lacking warm-based glaciers or other groundwater recharge pathways, such models do not seem applicable (Ballantyne, 2018; Grasby et al., 2014; Woo, 2012). An alternative model to explain the existence of perennial springs in such environments is that hydraulic head gradients in the sub-permafrost hydrogeological system are maintained by artesian pressure generated by past or current aggradation of basal

50 permafrost (Fig. 1). This would remove the need to invoke groundwater recharge from the surface. Furthermore, it might explain the formation of emergence-related open system pingos in coastal lowlands (Burr et al., 2009; Yoshikawa and Harada, 1995).

In this paper, we use field data from Adventdalen, Svalbard, in combination with numerical modelling of heat and groundwater transport to evaluate the hypothesis that perennial spring flow through continuous permafrost can be driven by

55 sub-permafrost artesian pressure produced by basal permafrost aggradation. Alternative causes of anomalous pressures are also discussed, including overpressure remaining from past perturbations (e.g. glacial loading) or contemporary processes such as equilibration of groundwater density contrasts and gas production. The investigation of the above hypothesis is based on decoupled heat and groundwater modelling, but in the discussion, this is combined with inverse analyses of spring geochemistry from a series of open-system pingos within the valley. A 1D heat transfer model forced by reconstructed paleo-

60 temperatures serves to simulate Holocene ground temperatures and permafrost development in the valley floor of Adventdalen. By considering the expansion of water upon freezing, the simulated rates of present permafrost aggradation must cause a loss

in aquifer volume equivalent to a recharge rate. This apparent recharge defines the only inflow term to a steady-state 3D groundwater model that simulates the present state of the sub-permafrost groundwater system. The modelling results are then discussed in relation to the hydrochemical observations of the pingo spring waters.

2   Conceptual model of permafrost aggradation-driven pingo formation

When permafrost aggrades into the ground, water in the pore space freezes, and hence expands. At shallower depths this is evident from ice lenses and other types of visible ground ice, resulting in ground heave, but from a certain depth downwards (e.g. ~ 5 m in Adventdalen: Gilbert et al., 2018), these cryostructures are no longer observed (French, 2017). Instead, the lithostatic pressure prevents ground heave and the ice expansion induces an overpressure (with regard to the hydrostatic pressure) on the sub-permafrost groundwater, especially where this cannot dissipate in an efficient manner. The process is well known from closed-system pingos, where groundwater is enclosed by aggrading permafrost and expelled to the surface from a closed talik (Mackay, 1998).

Liestøl (1977) suggests an open-system pingo-spring can be driven by recharge from subglacial melting of warm-based glaciers. Scheidegger et al. (2012) developed a coupled model of transient permafrost formation and showed how hydraulic heads can maintain the system for millennia even when permafrost is aggrading (disregarding ice expansion). In our study, we test the hypothesis that permafrost aggradation itself can generate such excess head.

Figure 1 illustrates our conceptual model for open-system pingo formation by basal permafrost aggradation and presents the additional conditions that also have to be met. The assumed starting point is a coastal landscape with no permafrost and a subsurface consisting of a hydrogeological unit in which hydraulic pressures dissipate poorly (Fig. 1a). Figures 1b and 1c illustrate that a negative shift in the surface energy balance results in permafrost aggradation. Freezing pressure is induced at the freezing front resulting in hydraulic head gradients. The shift in the surface energy balance may occur due to a drop in the MAAT (Figs. 1b–c), a regressing shoreline (Fig. 1c), rapid erosion (not illustrated), or a combination of any of these. Close to the sea, groundwater flows towards the shoreface, but at some distance inland, higher advective heat transfer, associated with higher groundwater velocities, prevents frozen ground formation and groundwater flows through an intra-permafrost talik (through-talik) towards the surface along the most hydraulically conductive path, and a spring (or pingo) forms (as modelled by Scheidegger et al., 2012). Freeze-up of the through-talik is further restricted if permafrost aggradation lowers the melting point by increasing pressure and/or salinity. Figure 1d illustrates that when ground temperatures are eventually in equilibrium with the MAAT, permafrost aggradation has stagnated, and groundwater flow to the pingos has ceased. Due to the lack of advective heat transfer, the through-talik might close and, if so, irreversibly de-activate pingo spring discharge (although salinity may keep the through-talik open, in spite of no-flow).
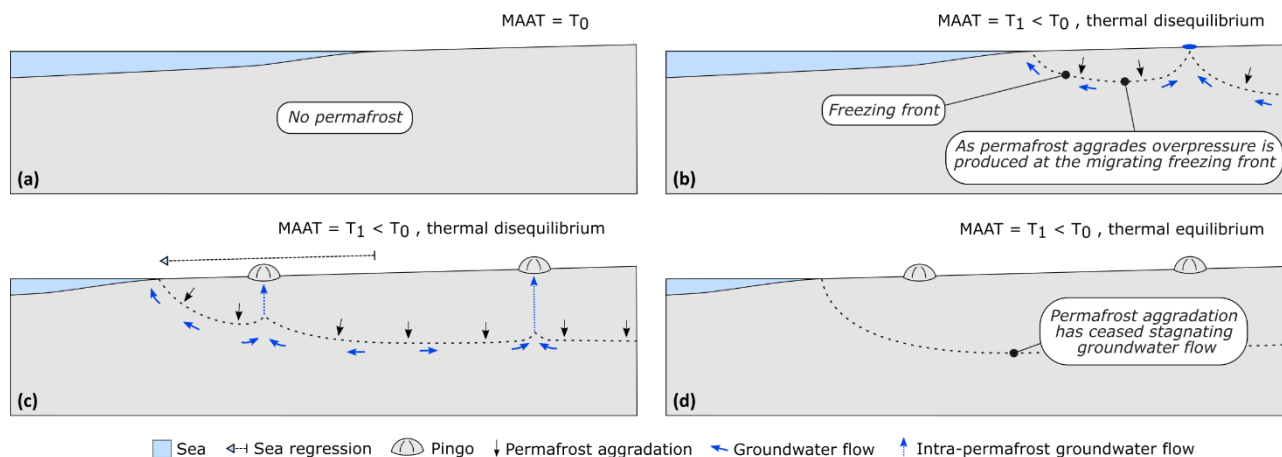
Figure 1 Conceptual model of pingo formation driven by permafrost aggradation in a low-permeable system. **(a)** No permafrost is present. **(b)** and **(c)** A negative shift in the surface energy balance results in permafrost aggradation. Freezing pressure is induced at the freezing front resulting in hydraulic head gradients. At some distance inland, higher advective heat transfer, associated with higher groundwater velocities, prevents the ground from freezing and groundwater flows to the surface and a spring (or pingo). **(d)** The ground is in thermal equilibrium with the MAAT, permafrost aggradation has stagnated, and groundwater flow to the pingos has ceased.

3   Field site and data

Adventdalen is a ~ 30 km long glacially cut valley in central Spitsbergen, Svalbard (Fig. 2a). Its high Arctic climate is characterised as polar tundra (Kottek et al., 2006) and the ground is dominated by continuous permafrost (Humlum et al., 2003). Because of the dry climate with a mean annual precipitation of ~ 200 mm (Hanssen-Bauer et al., 2018) only a few, small glaciers exist today, the largest being Drønbreen, 9 km long and up to 200 m thick.
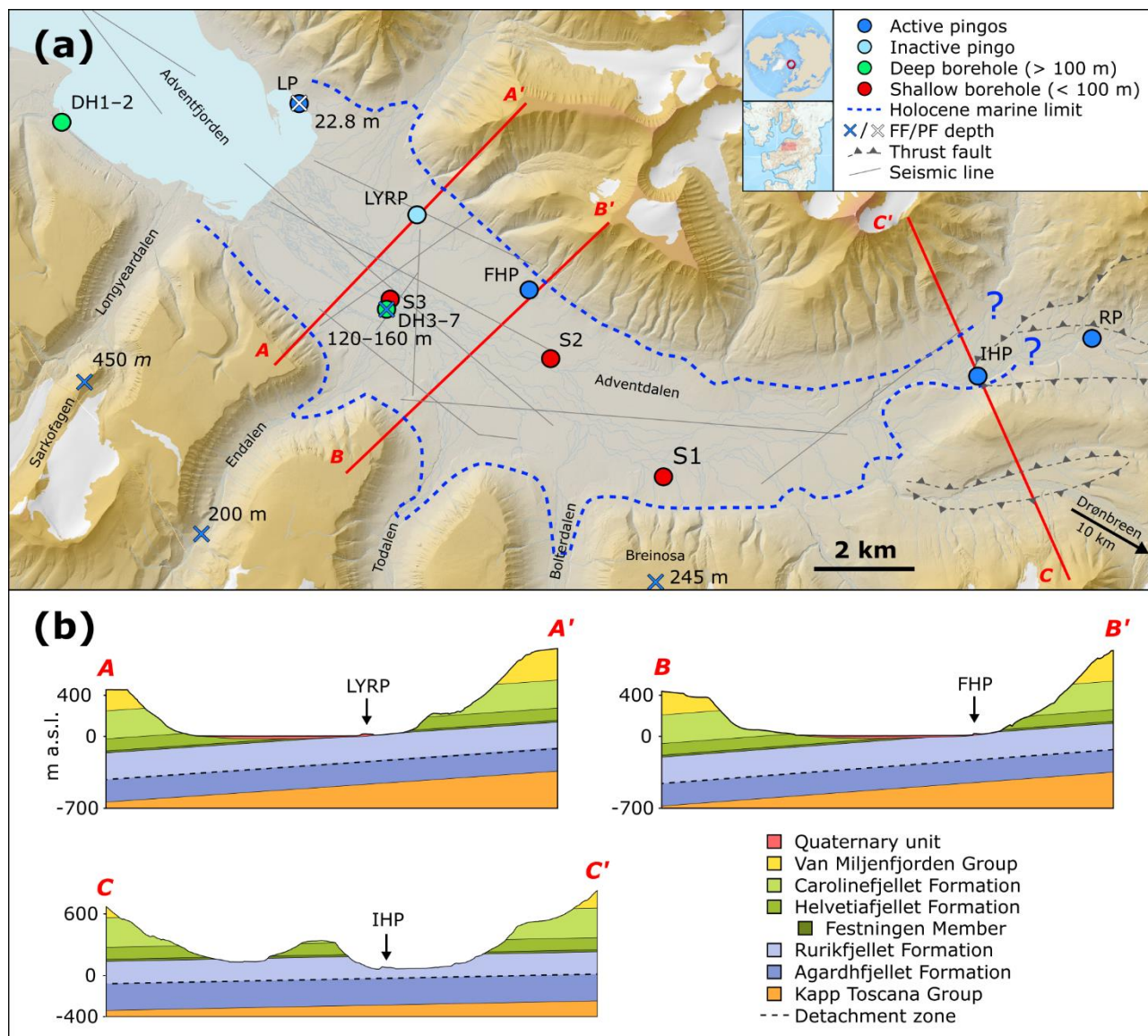
Figure 2 (a) Map of Lower Adventdalen with the location of data resources, pingos and the Holocene marine limit. LP=Lagoon Pingo,
LYRP=Longyear Pingo, FHP=Førstehytte Pingo, IHP=Innerhytte Pingo, RP=River Pingo. Core logs from boreholes S1–3 and D1–D7
(respectively, Gilbert et al., 2018, and Olaussen et al., 2020, and references therein), seismic lines (Bælum et al., 2012, and unpublished
commercial lines from Norsk Hydro) and a geological map (Norwegian Polar Institute, 2019) were used to build the geological model (Fig.
4) (see details in Hornum, 2018). Permafrost depths (temperature logging) are from Liestøl (1977) (Sarkofagen), Braathen et al. (2012)
(DH4), and (Christiansen et al., 2005) (Breinosa). The freezing front depth (geophysics) is from Yoshikawa and Harada (1995). Map data
by courtesy of Norwegian Polar Institute (2019). **(b)** Geological cross sections constructed based on the resources mentioned above. See
Sect. 3.1 for a (hydro)geological description.

3.1   Geology and hydrogeology in Adventdalen

As illustrated on Fig. 2b, fine-grained Quaternary sediments (< 70 m thick Gilbert et al., 2018) overly pre-Cenozoic, well-consolidated sedimentary strata in Adventdalen, which are likely the best described in Svalbard largely thanks to the
115   Longyearbyen CO2 Laboratory Project (Olaussen et al., 2020, and references therein). Together, these form a low-permeability groundwater system.

The sedimentary strata gently dip in a west-south-westerly direction (Fig. 2b) and the youngest strata are thus found closest to Longyearbyen and the present-day coastline. The uppermost unit, the Early Cretaceous Carolinefjellet Fm (~ 300 m thick, Fig. 2b), consists of sandstone intercalated with shale beds and overlies the fluvial sandstones of the Helvetiafjellet Fm
120   (59–72 m thick, Grundvåg et al., 2019). The Festningen Member of the Helvetiafjellet Fm (11–18 m thick), comprises fractured sandstones and is relatively hydraulically conductive, as proven by cross-well water injection tests (Bælum et al., 2012). Directly below is the ~ 450 m thick Janusfjellet Subgroup (Fig. 2b) that comprises two shale-dominated units, the Rurikfjellet (201–232 m thick, Grundvåg et al., 2019) Agardhfjellet Formations (253–264 m thick, Koevoets et al., 2018). A regional detachment zone with extensive fracturing and swelling clays propagates near the boundary of these two formations (Braathen
125   et al., 2012) and is considered the main seal for the potential of CO_2 storage (Olaussen et al., 2020). The tectonic disturbances, as reflected in Festningen Sandstone and the detachment zone, makes it possible that minor secondary permeability development is present elsewhere in the stratigraphy. This would have implications for groundwater movement in the system, which is otherwise predominantly through rocks with low hydraulic conductivity (Table 3).

The glacier advances during the last glacial maximum (LGM) on Svalbard (~ 20 ka (10^3 yr BP)) are thought to have
130   completely eroded any pre-existing glacial deposits in the inner fjords of Svalbard (Elverhøi et al., 1995) and the Quaternary succession in Adventdalen thus postdates this event. OSL datings in three cores from Adventdalen (S1, S2, and S3, Fig. 2a) support this (Gilbert et al., 2018). The Quaternary succession overlies fractures in the underlying sedimentary strata, possibly explained by glacier load/unload and freeze-thaw processes (Benn and Evans, 2010; Gilbert et al., 2018), as well as the significant tectonic uplift in the area. The presumed high hydraulic conductivity of this fracture zone is in contrast to generally
135   low-permeable sediments of the Quaternary succession: The lowermost Quaternary unit is a < 5 m thick, subglacial lodgement till deposited during the last Weichselian glacial advance. Overlying the till, a shallowing-upwards trend is observed in the gradually changing succession of marine muds (< 20 m), pro-deltaic to deltaic muds and very fine-grained sands (< 35 m), tidally influenced (saline) fluvial fine-grained sands (< 35 m), and aeolian loess deposits (< 5 m). This reflects Holocene progradation of the present delta-system (Cable et al., 2018; Gilbert et al., 2018).

140   The sub-permafrost groundwater often has hydraulic heads above hydrostatic, which results in artesian conditions. This is evident from the occurrence of several pingo springs and from artesian outflow from deep boreholes (> 100 m below ground level (b.g.l.)) at the confluence of Bolterdalen and Adventdalen (Malte Jochmann, pers. comm.; SNSK, Unpublished Reports SN1981_008 and SN1983_004). Nearby, Braathen et al. (2012) deduce a hydraulic pressure of 18 to 23 bars at a depth of ~ 175 m b.g.l. in well DH4 (Festningen Member, Fig. 2), which corresponds to a hydraulic head of 9 to 60 m above

145 hydrostatic when the potential pressure effects of the dissolved gasses are excluded. Significant under-pressure ~ 50 bar below hydrostatic is recognised in deeper stratigraphical layers (~ 800 m b.g.l.) and is believed to relate to glacial unloading, extensive fracturing and matrix expansion (Birchall et al., in review.; Braathen et al., 2012; Wangen et al., 2016). The low pressure indicates hydrogeological separation from upper groundwaters immediately beneath the permafrost, in line with Sr-isotope analyses from the drill cores (Huq et al., 2017; Ohm et al., 2019).

150 **3.2   Late Weichselian and Holocene climate history**

Air temperatures on Svalbard have been continuously recorded at Longyearbyen Airport since 1911 (Nordli et al., 2014). Until the 1990s, the 30-yr running mean of mean annual air temperatures (MAAT) was -6.0 °C, while it has increased to -4.2 °C in the period 1988 to 2017 (Hanssen-Bauer et al., 2018). The mean summer air temperature (MSAT) has consistently been 10 °C warmer than the MAAT (on the 30-yr scale, Førland et al., 1997).

155   Holocene temperatures on and around Svalbard are relatively well constrained by fossil-based temperature reconstructions. Mangerud and Svendsen (2017) infer a mean summer sea temperature (MSST) curve from the distribution and ^{14}C–dating of thermophilous bivalves and point out that the MSST is essentially identical to the MSAT. As illustrated on Fig. 3a, their MSST curve is largely in agreement with MSST temperature reconstructions from west and southwest of Svalbard (van der Bilt et al., 2018; Hald et al., 2007). Assuming that the present difference between MAAT and MSAT was alike for

160 the entire Holocene, we use a MAAT reconstruction inferred by subtracting 10 °C from the MSST curve by Mangerud and Svendsen (2017) for the modelling of ground temperatures in this work (Fig. 3b). We choose to rely on Mangerud and Svendsen (2017) because; a) their curve is more local to our field area than the alternatives and; b) the suggested timing of the Holocene thermal minimum at ~ 3 to 2 ka is in agreement with the maximum of perennial or semi-permanent land fast sea ice at ~ 2.5 to 2 ka inferred from the minimal occurrence of dated driftwood (Dyke et al., 1997; Farnsworth, 2019; Funder et al.,

165 2011). Furthermore, their curve is better supported by geomorphological evidence of glacier dynamics (Farnsworth, 2019).

Table 1	*Absolute ages from Adventdalen constraining delta propagation*			
Site/*Event	**Distance to modern delta front [m]**	**Dating method**	**Dating material**	**Age of valley floor [yr BP]**
LP	~340	C-14	Peat	> 240 (±50)[I]
LYRP	~3650	C-14	Driftwood	< 2650 (±55)[II]
S3	~4300	Quartz OSL	Quartz	~ 3000 (±200)[III]
FHP	~6400	C-14	Shell	< 6980 (±70)[IV]
S2	~7500	C-14	Plant matter	< 9178 (±153)[III]
HML	~16000	C-14	Shell	< 10025 (±160)[V]

See Fig. 2 for site locations. HML = Holocene marine limit. Compiled from [I]Åhman (1973), [II]Svensson (1970), [III]Gilbert et al. (2018), [IV]Yoshikawa and Nakamura (1996) and [V]Lønne and Nemec (2004).
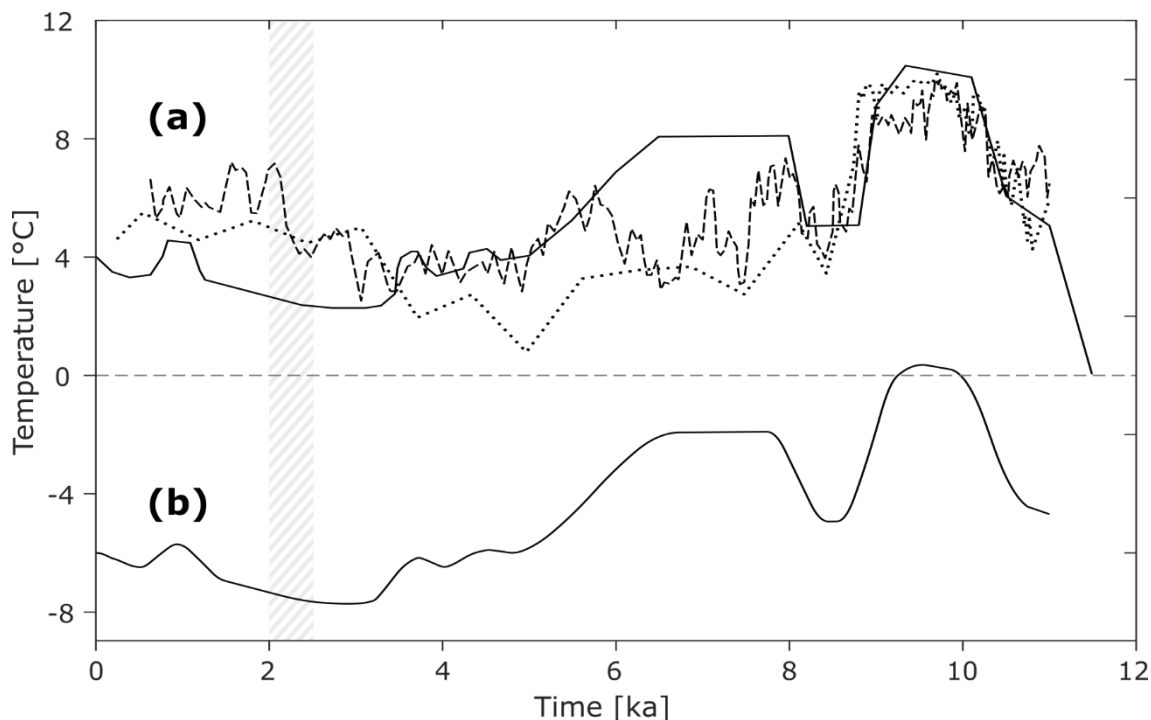
Figure 3 Holocene temperature reconstructions. Dashed light grey area indicate time of minimal driftwood arrival (Farnsworth, 2019). **(a)** MSST curves (= MSAT, see text). Solid line from Mangerud and Svendsen (2017). Dotted line from Hald et al. (2007). Dashed line from van der Bilt et al. (2018). **(b)** MAAT used in this work. Based on Mangerud and Svendsen (2017) and Førland et al. (1997).

At the last glacial maximum (LGM) occurring at ~ 20 ka, glaciers covered all fjords in Spitsbergen (Ingólfsson and Landvik, 2013). By ~ 11.5 ka the central parts of Isfjorden were glacier-free and its inner tributaries followed at ~ 11.2 ka (Forwick and Vorren, 2011; Gilbert et al., 2018). If any glacier ice remained in Adventdalen after then, it was certainly gone by ~ 10 ka when non-glacial sediments were deposited in the valley head (Lønne and Nemec, 2004). The eustatic sea-level rise caused by northern hemispheric deglaciation during Late Quaternary and Early Holocene was surpassed on Svalbard by the rate of its postglacial rebound. The Holocene marine limit (HML) ranges from ~ 20 m above sea level (a.s.l.) in the northwestern part of Spitsbergen to ~ 90 m a.s.l. in the central part (Forman, 1990). In Adventdalen, raised marine sediments suggest a HML of ~ 62 m a.s.l. and ~ 70 m a.s.l. in the inner and outer part of the valley, respectively (Lønne and Nemec, 2004). Although not well constrained, the relative sea level is estimated to have fallen pseudo-exponentially until reaching close to present levels ~ 5 ka (Lønne and Nemec, 2004). Despite the uncertainty of sea-level fall, the fjord retreat and the associated exposure of new valley floor are relatively well constrained by absolute dating presented in previous work (Table 1). Depending on the dated material and the host sediment, the dating indicates minimum, approximate or maximum ages of subaerial exposure (i.e. exposure to MAATs).

3.3   Permafrost, pingos and the apparent lack of groundwater recharge

In the valley floor of Adventdalen, the permafrost thickness ranges from ~ 0 m at the coast to ~ 200 m inland. In the adjacent
190   mountains it increases to > 450 m (Christiansen et al., 2005; Humlum et al., 2003; Liestøl, 1977). Specific depth observations
support this regional characterisation (Fig. 2a). Mountain permafrost is presumably of Weichselian age, while permafrost in
valleys postdates the Late Holocene (Humlum, 2005). The continuous permafrost and a lack of warm-based glaciers in the
adjacent highlands most likely hinder subglacial recharge to the sub-permafrost aquifer due to the impervious frozen ground
(Burt and Williams, 1976; McCauley et al., 2002; Walvoord and Kurylyk, 2016; Woo, 2012).

195   Sub-zero temperatures are a prerequisite for permafrost formation and its thickness essentially reflects equilibration
to the geothermal heat flow (French, 2017). In the Adventdalen area, measurements of the geothermal gradient range from
0.02 °C m^{-1} in the highlands to 0.03 °C m^{-1} in the valley bottoms (Betlem et al., 2019; Liestøl, 1977).

Open-system pingos are a common feature in Svalbard and Adventdalen (Humlum et al., 2003), where five of them
are distributed parallel to the valley axis (Fig. 2a). The three outermost; Lagoon, Longyear and Førstehytte Pingos, are all
200   located on the northeastern side of the valley. All three have formed in Quaternary marine muds (Yoshikawa and Harada,
1995) and close to the sedimentary bedrock boundary (Fig. 2b). In the valley head, two additional pingos are located close to
the boundary of HML; Innerhytte and River Pingos. They have formed in shales above a major fault and are situated in the
valley floor in the path of the river Adventelva (Yoshikawa and Harada, 1995). With the exception of the seemingly inactive
Longyear Pingo, groundwater has discharged perennially from springs located at the pingos, at least since the earliest
205   recordings in the 1920s (Orvin, 1944). However, visible spring outflow (or winter icing) at Førstehytte Pingo was not observed
from summer 2018 until October 2019. Presumably, during that time, groundwater flow through the permafrost continued, but
instead of discharging to the surface, groundwater froze within the pingo and added to its growth. From Lagoon Pingo,
Yoshikawa and Harada (1995) reported a spring discharge of 0.013 to 0.016 L s^{-1}, Hodson et al. (2019) estimated ca. 0.3 L s^{-1}
during the 2017 summer, and we measured 0.26 L s^{-1} in August 2019. At Innerhytte Pingo, Yoshikawa and Harada (1995)
210   measured a discharge rate of 0.11 L s^{-1}, which is somewhat smaller than Liestøl's (1977) estimate in 1976 of ~ 1 L s^{-1}. Based
on our own "by the eye" observations, the discharge rate at Førstehytte Pingo was closer to 0.1 L s^{-1} when visited in fall of
2015, 2016 and 2017, and less than 0.01 L s^{-1} when rediscovered in October 2019.

4   Numerical modelling

Several numerical model codes are capable of simulating coupled heat and groundwater transport in permafrost environments
215   (Grenier et al., 2018). However, the benchmark models do not consider the overpressure produced by ice expansion. To include
this process, we decoupled the modelling of heat flow from sub-permafrost groundwater flow and made use of a source term
to mimic the pressure effects of permafrost aggradation. Ground temperatures and permafrost dynamics were simulated in the
vertical dimension using a custom made finite-difference 1D transient heat transfer model (hereafter just 1DHT) coded in
MATLAB R2018b (MathWorks®, 2019). The 1DHT model script is publicly available at DOI:10.5281/zenodo.3578839.

220   Groundwater flow was modelled 3D steady-state with MODFLOW in GMS 10.4 (AQUAVEO™, 2019). The connection

between the two models was the permafrost aggradation rates simulated by the 1DHT, which determined the only water source

for the groundwater model. A schematic overview of the modelling approach is provided in the Supplement. The decoupled

approach does not simulate advective nor lateral heat transport. The potential limitations will be assessed in the Discussion

(Sect. 6.2.1).

225   **4.1   Heat flow**

Heat flow was modelled one-dimensionally in the vertical dimension, which is a common approach for permafrost models

(Riseborough et al., 2008). Following from Fourier's law and conservation of energy, the 1D conductive heat flow equation

states that:

$$\frac{\delta T}{\delta t} = \frac{k_e}{\rho_e \cdot c_e} \cdot \frac{\delta^2 T}{\delta z} \qquad (1)$$

230   where T is temperature [K], t is time [s], z is distance [m], and k_e, ρ_e, and c_e are the effective values of the thermal conductivity

[W (m K)$^{-1}$], density [kg m^{-3}], and specific heat capacity [J (kg K)$^{-1}$], respectively. The term $\frac{k_e}{\rho_e \cdot c_e}$ equates to α_e, the effective

thermal diffusivity [m^2 s^{-1}]. As heat transfer was modelled one-dimensionally, simulating advective heat transfer was not

possible. The ratio of advection to conduction heat transfer rates may be quantified by a Peclet number (Bergman et al., 2011):

$$P_{e_L} = \frac{v \, L}{\alpha_e} \qquad (2)$$

235   where v is the pore water velocity and L is the characteristic length.

In the case of a saturated medium, heat conduction will flow through a matrix of sediments or rocks and H_2O

as water, ice or a mixture. The effective thermal parameters were assumed independent of temperature, but the fractions of

water and ice changed between the solidus and liquidus temperatures, T_S and T_L respectively. The fraction of water within the

pore space, f_w, was determined using a smoothed step function (same approach as Mottaghy and Rath, 2006):

240
$$f_w = \begin{cases} \exp\left(-\left(\frac{T-T_L}{w}\right)^2\right) & if \;\; T < T_L \\ 1 & if \;\; T > T_L \end{cases} \qquad (3)$$

where w [K] determines the shape of the freezing curve. For this work $w \approx 0.96$, implying that $T_S = $ -2 °C and $T_L = 0$ °C.

Bonacina and Comini (1973) and Mottaghy and Rath (2006) note that the exact shape of the freezing curve is of little

importance for the calculated temperatures, but that a smoother function generally improves the performance of a numerical

model due to a more efficient convergence of the numerical approximation. The total fractions of soil or rock (F_s), water (F_w),

245   and ice (F_{ice}) are described respectively as; $F_s = 1 - n$, $F_w = f_w \cdot n$, and $F_{ice} = n - F_w$ with n being the total porosity. The

effective thermal conductivity was calculated as root-square-mean, as done by Mottaghy and Rath (2006) and Govaerts et al.

(2016). When temperature change occur between T_S and T_L, freezing or thawing results in the release or absorption of latent

heat, $L = 333.6$ kJ kg^{-1} (Mottaghy and Rath, 2006). The latent heat of fusion was included in the expression of the equivalent

volumetric heat capacity [J (m^3 K^{-1}], C_{eq} (same approach as Govaerts et al., 2016):

250
$$C_{eq} = c_e \cdot \rho_e = F_s \cdot \rho_s \cdot c_s + F_w \cdot \rho_w \cdot \left(c_w + \frac{\delta f_w}{\delta T} \cdot L\right) + F_{ice} \cdot \rho_{ice} \cdot \left(c_{ice} + \frac{\delta f_w}{\delta T} \cdot L\right)$$ (4)

where subscripts s, w, and ice indicate parameters of soil or rock, water, and ice, respectively.

To validate the model code we compared simulations with two analytical solutions; Neumann's solution as presented by Carslaw and Jaeger (1959) and Mottaghy and Rath (2006); and an analytical solution of a step change in temperature neglecting latent heat effects as presented by Carslaw and Jaeger (1959) and Eppelbaum et al. (2014). The model
255   code validation is described in detail in the supplementary info.

4.2   Groundwater flow

Following from Darcy's law and the conservation of mass, the 3D groundwater flow equation fundamental for groundwater modelling can be described as (Fitts, 2002):

$$K_x \frac{\delta^2 h}{\delta x^2} + K_y \frac{\delta^2 h}{\delta y^2} + K_z \frac{\delta^2 h}{\delta z^2} + Q_N = S_s \frac{\delta h}{\delta t}$$ (5)

260   where x, y and z are distances [m] in the three dimensions, K's are hydraulic conductivities [m s^{-1}] in those dimensions, h is the hydraulic head [m], Q_N is a term representing any potential sink or source [m^3 s^{-1}] (i.e. recharge, seepage, etc.), S_s is the specific storage, and t is time [s]. In this work, groundwater flow was modelled as a steady-state implying that the right-hand side of Eq. (5) equals 0. However, in the discussion of the model simulation results, hydrodynamic storage effects resulting from the glacial loading and unloading are considered.

265   Groundwater flow was simulated with MODFLOW, which solves the 3D groundwater flow equation with the finite-difference method (McDonald and Harbaugh, 1988). We approximated the pressure build-up from the simulated rate of permafrost aggradation, R_{PF}, by considering that it must correspond to some equivalent recharge rate (or source term, Q_N in Eq. 5), REq. Assuming no expansion or compression of the matrix, REq is specifically proportional to R_{PF}, the total porosity, n, and the expansion of water upon freezing, X_w:

270   $$REq = R_{PF} \cdot n \cdot X_w$$ [m s^{-1}]   (6)

$$Q_{REq} = REq \cdot A$$ [m^3 s^{-1}]

where Q_{REq} is equivalent to the source term Q_N in Eq. (5).

4.3   Setup and boundary conditions

4.3.1   Geological model

275   In order to define proper geothermal and hydrogeological properties, a geological model of the subsurface in Adventdalen was built. The horizontal model boundary was a simplified outline of the valley bottom and the lower boundary was at 300 m b.g.l. (Fig. 4). We used data from boreholes, seismic lines (see locations and references on Fig. 2a), and a geological map with DEM provided by the Norwegian Polar Institute (2019). The general workflow was to map relevant geological boundaries in 3D with the petroleum industry software Petrel v2016 (Schlumberger©, 2019), then used them to build geological layers with the

280 TIN and SOLIDS editor functions in the groundwater modelling software GMS v10.4 (AQUAVEO™, 2019). For the 1DHT model, the geology was simplified into one-dimensional columns for a total of 12 subzones defined based age of the valley floor (Table 1).
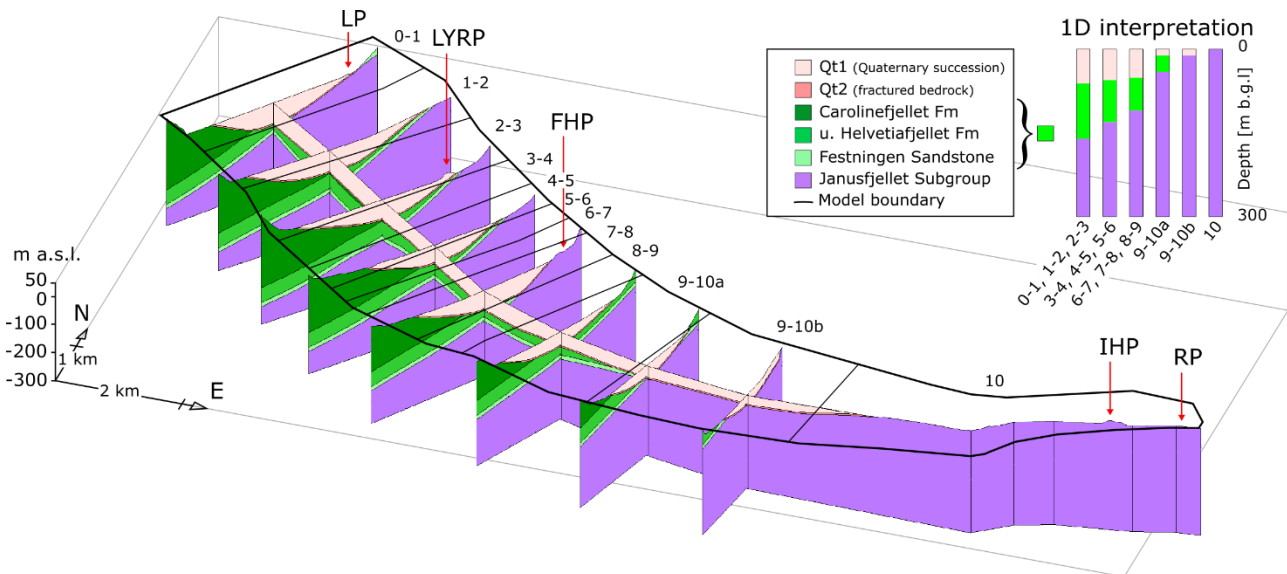
285 **Figure 4** 3D geological model of subsurface below the valley floor in Adventdalen and vertical 1D simplifications below subzones of the model area. The former determines the hydrogeological properties in the groundwater model (Table 3), whereas the latter determines the geothermal properties in the 1DHT model (Table 2). The subzones were defined based on the reconstruction of fjord retreat and their names indicate the exposure ages (i.e. zone 0-1 became sub-aerially exposed between 1 and 0 ka, zone 1-2 between 2 and 1 ka, etc.).

4.3.2 Geothermal and hydrogeological properties

290 Due to the sparse data available from the field area, geothermal and hydrogeological properties of the lithologies in the model domain (Tables 2 and 3) were largely based on typical values found in the literature. An exception was the measurements of porosity and vertical permeability, κ_v, in the sandstone units carried out by the Longyearbyen CO_2 Laboratory Project (Olaussen et al., 2020, and references therein). Porosity was found to be the most important parameter for permafrost growth, and realistic minimum, mean, and maximum values were therefore defined for the 1DHT model (Table 2). The small-scale

295 horizontal permeability, κ_h, for sandstones is typically a factor two higher than κ_v (Domenico and Schwartz, 1998). The horizontal hydraulic conductivity, K_h, was therefore calculated using the measurements of κ_v by Braathen et al. (2012) as

$$K_h = C_{Kh/Kv} \cdot \frac{\kappa_v \cdot \rho_w \cdot g}{\mu} \qquad (7)$$

where $C_{Kh/Kv}$ is the conversion factor (i.e. 2 for this work), κ_v is permeability [m²], ρ_w is the density of water [kg m⁻³], g is the gravitational acceleration [m s⁻²], and μ is the dynamic viscosity of water [kg (m s) ⁻¹]. Ranges of hydraulic conductivity

300 for the fluvio-deltaic succession were based on literature values from (Fitts, 2002). For the bedrock units we also regarded the

influence of fractures (Singhal and Gupta, 2010). All within these ranges, three sets of hydraulic conductivity defined the different model scenarios Sc1–3 (Table 3). For steady-state simulations, the porosity does not affect the net groundwater fluxes (i.e. discharge and Darcy fluxes, Eq. 5). To evaluate the pore water velocities, however, the effective porosity is of importance. We used the same values of effective porosity for all groundwater model simulations (Table 3).

305

Table 2		*Geothermal properties*				
Material	**Thermal conductivity** [J (yr m K)$^{-1}$]	**Specific heat capacity** [J (kg K)$^{-1}$]	**Density** [kg m^{-3}]	**Total porosity** [m^3 m^{-3}]		
				Min	Mean	Max
Water	1.77·10^7	4180	1000	-	-	-
Ice	7.06·10^7	2100	917	-	-	-
Silty sand (Qt)	1.58·10^7	850	2400	0.3[I]	0.4[I]	0.5[I]
Sandstone	7.88·10^7	900	2600	0.06[II]	0.1[II]	0.15[II]
Shale	4.73·10^7	800	2600	0.1[III]	0.2[III]	0.3[III]

Density and thermal properties compiled from Bergman et al. (2011) , Williams and Smith (1989), Farouki (1981), and Robertson (1988). Porosities from [I]Fitts (2002), [II]Braathen et al. (2012), and [III]Manger (1963).

Table 3		*Hydraulic conductivity* [m day^{-1}]			*Effective porosity*
Hydrogeological unit	**Lithology**	**Sc1**	**Sc2**	**Sc3**	**All**
Qt1	Clay, silt and sand	10^{-4}	10^{-3}	10^{-2}	0.4
Qt2	Heavily fractured bedrock	10^{-2}	0.1	1	0.4
[1]Carolinefjellet Fm	Sandstone	10^{-4}	10^{-3}	10^{-2}	0.1
[1]u. Helvetiafjellet Fm	Sandstone	10^{-4}	10^{-3}	10^{-2}	0.1
Festingen Sandstone	Fractured sandstone	10^{-2}	5·10^{-2}	0.1	0.1
Janusfjellet Subgroub	Shale	10^{-4}	5·10^{-4}	10^{-3}	0.1
Detachment zone	Fractured shale	10^{-3}	5·10^{-3}	10^{-2}	0.1

[1]Evaluated from Braathen et al. (2012). The remainder based on Fitts (2002) and Singhal and Gupta (2010).

310 **4.3.3   1D transient heat transfer model (1DHT)**

The model domain contained 12 one-dimensional grids, each 300 m long and consisting of 150 cells with a height of 2 m. Each individual grid was associated to the model area zones (Fig. 4) and the geothermal properties were defined accordingly. The names of the zones refer to the age of subaerial exposure (Table 1), which defined the simulation run time (e.g. for zone 0-1 the simulation period was 0.5 to 0 ka, for zone 1-2 it was 1.5 to 0 ka, etc. For zone 10, the simulation period was 10 to 0

315 ka). The initial ground temperature distribution followed the geothermal gradient reported by Liestøl (1977) (0.025 °C m^{-1}) from a surface temperature of 0 °C. At any subsequent time, the lower boundary condition was defined from the same geothermal gradient. The Holocene temperature curve (Fig. 3) defined the upper boundary condition.

4.3.4   Groundwater model

Each grid cell measured 100 by 100 by 5 m (*x y z*) and their hydrogeological properties were defined from the geology (Fig.

320 4, Table 3). The model domain was defined from the geological model therefore covering an elongated ground surface area of 59 km^2 that is < 4 km broad and ~ 18 km long (Fig. 4). Frozen ground was considered impervious and cells shallower than the simulated freezing front depth were thus inactivated. The lower boundary was at 300 m b.g.l. The fjord was simulated with a

general head of 0 m a.s.l. assigned to the relevant cells and the conductance was determined according to hydraulic conductivity (Table 3). The MODFLOW drain package was used to simulate pingo springs. Because the cells located at the springs were

325 inactivated, the drains were assigned to the uppermost active cells located closest to springs, but within the conductive Festningen Sandstone. Drain levels were set according to spring elevations (i.e. 1, 20, 65, and 77 m a.s.l. for Lagoon, Førstehytte, Innerhytte, and River Pingos, respectively). The simulated springs were able drain more water than the cells they were situated in could transmit. That is, the conductance was set more than high enough not to restrict any discharge. Except for the fjord and the springs, all outer model boundaries were no-flow conditioned.

330 **5.1   1DHT model results**

The raw simulation results from the 1DHT model were matrices containing the temperatures throughout the model domain for each time step in the simulation period. The evolution of the permafrost and freezing front depths were evaluated by interpolating the associated temperatures for each time step. The greatest phase change rate in the 1DHT model occurs at a temperature of -0.7 °C (following from Eq. 3) and the (always) downwards progression rate of this isotherm was therefore

335 used for the calculation of the equivalent recharge (by net pore space loss, Eq. 6). Since phase change occurs over a temperature range, the porosity used to calculate the equivalent recharge was taken as a weighted mean of the porosities in the corresponding cell range, where the weight was proportional to the phase change rate.

5.1.1   Permafrost and freezing front depth

In Fig. 5, the simulated Holocene ground temperature development in Adventdalen is exemplified by the growth of frozen

340 ground and permafrost in zones 2-3, 7-8 and 9-10b when using the intermediate porosity values (Table 2). For the oldest part of the model area (most inland), an early occurrence of frozen ground was simulated during the Early Holocene cooling of 9 to 8 ka (Figs. 3 and 5). However, due to the subsequent warming at 8 to 6.5 ka, frozen ground was thawed and not reestablished until ~ 6.5 ka. Since this time, deep ground temperatures were simulated to be cooling until present. The pattern was identical for simulations with lower and higher porosities (not shown) although the depths were different (as illustrated on Fig. 6).
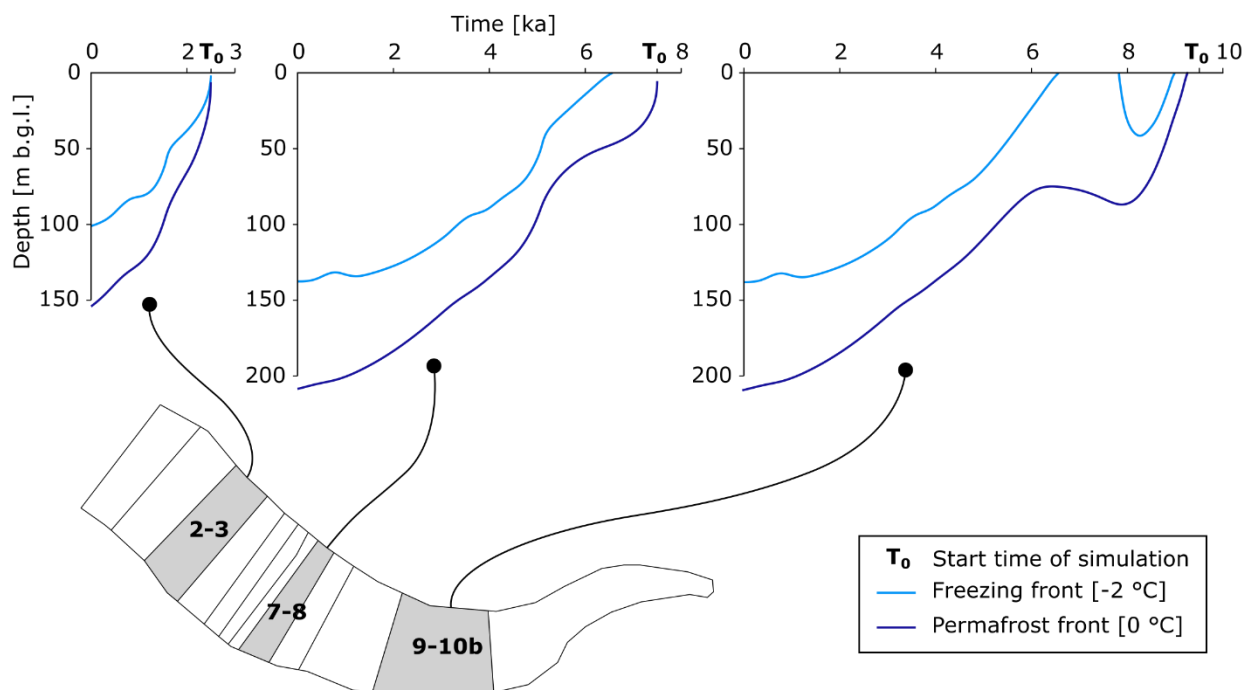
345

Figure 5 Development of simulated freezing front and permafrost front depths from zones 2-3, 7-8 and 9-10b (Fig. 4). These simulation results derive when using the intermediate porosity values (Table 2). Note that completely frozen ground does not establish permanently until ~ 6.5 ka.

Depending on the scenario, the 1DHT model simulated present day permafrost and freezing front depths of respectively 192
350   to 232 and 125 to 155 m b.g.l. at distances further than 6 km from the delta front (Fig. 6). Closer to the delta front both isotherms are located at shallower depths and decrease to 58 to 64 m b.g.l. and 31 to 34 m b.g.l. The porosity plays an important role for the temperature development due to latent heat of the water (ice) filling the pore space and because water and ice account for the minimum and maximum, respectively, thermal diffusivities in the model domain. In panel (a) and (c) of Fig. 6, an uncertainty field is drawn (shading) as derived from the applied porosity range (Table 2). The upper and lower edge of
355   the shaded area corresponds to the maximum and minimum porosity. The line corresponds to the intermediate porosity (Table 2). The scarcity of ground temperature observations does not allow for model calibration, but observations both at Lagoon Pingo (freezing front) and well DH4 (permafrost) agree relatively well with simulations.
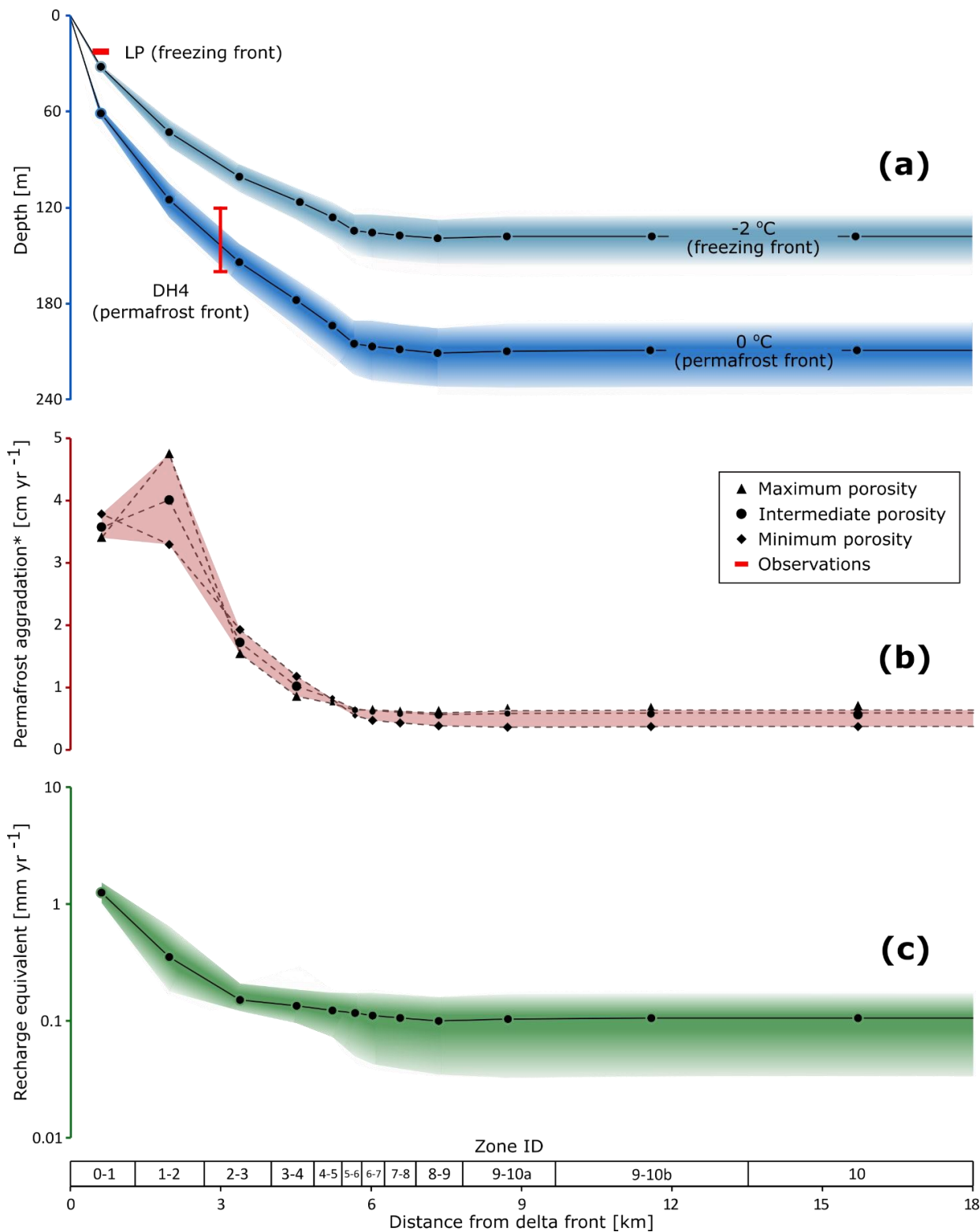
360 **Figure 6** (previous page) Present-day permafrost conditions as simulated by the 1DHT model. For both **(a)** and **(c)**, an uncertainty field is illustrated with shading. The upper and lower edge of the shaded areas corresponds to the maximum and minimum limits of the porosity range, while the curve and the points corresponds to the intermediate (Table 2). **(a)** Freezing front and permafrost depths. **(b)** Rate of permafrost aggradation. *It is the -0.7 °C isotherm, which has been used to calculate this as the greatest phase change rate takes place at that temperature. **(c)** Equivalent recharge rate (net rate of loss in pore space). The points on the curve and the outer edges of the shaded area
365 represent the values, which were assigned to the corresponding zones in the groundwater model.

5.1.2   Permafrost aggradation and recharge equivalent

Simulated rates of present permafrost aggradation ranged from $5 – 0.5$ cm yr^{-1} and generally decreased up-valley with older exposure ages (Fig. 6b). At first surprising, the model simulations generally did not suggest the highest aggradation rate occurred where permafrost is youngest (zone 0-1), but instead at zone 1-2 (the exception was the simulation with the lowest
370 porosities in Table 2). This was due to the different properties of the sediments and bedrock undergoing freezing (Fig. 4). In zone 0-1, closest to the shore, phase change took place at < 60 m b.g.l. corresponding to the most porous and least thermally diffusive unit (the fluvio-deltaic succession). Thus, a relatively high amount of latent heat had to be released for the freezing front to aggrade. By contrast, the opposite was the case in zone 1-2, where the freezing front just entered the sandstone unit that possessed the lowest porosity. For the same reason, Fig. 6c shows that the pattern of the equivalent recharge decreases
375 from $1 – 1.5$ mm yr^{-1} closest to delta front (zone 0-1), to $0.04 – 0.15$ mm yr^{-1} in zone 10 furthest up-valley. Fig. 6 also shows the permafrost and freezing front depths, with the uncertainty range derived from the application of the range in porosity values.

5.2   Simulated aquifer flow paths and flow velocity distributions

The above simulated recharge equivalent rates were assigned to cells within the corresponding zones of the model area (Fig.
380 4). The resulting outputs of the groundwater model for all scenarios are shown in Fig. 7. The equivalent recharge rates, REq, calculated from the 1DHT model simulations resulted in a total inflow of water, Q_{REq} to the groundwater system of 25.4, 40.6 and 56.7 m^3 day^{-1}, respectively, for the maximum, intermediate and minimum porosity scenarios. These values correspond to average recharge rates of 0.16, 0.25 and 0.35 mm day^{-1} if distributed over the entire model area.

Simulated hydraulic heads ranged from sea level to maxima of either 406 m a.s.l. (maximum Q_{REq} and minimum K
385 scenario, Fig. 7-1c) or 28 m a.s.l. (minimum Q_{REq} and maximum K scenario, Fig. 7-3a). For all of the minimum K scenarios (Figs. 7-1a–c), the simulated hydraulic head in well DH4 was significantly higher than observed. The simulated head fell slightly below the lowest end of the range of the observed head in the scenario with minimum Q_{REq} and maximum K (Fig. 7-3a). For the remaining five scenarios, the groundwater model simulated heads within the uncertainty range of the observation (Figs. 7-2a–c and 7-3b–c). Entirely or almost entirely artesian conditions were simulated for all but three scenarios (small Q_{REq}
390 and high K, Figs. 7-2a and 7-3a–b), where the up-valley part of the system has hydraulic pressures below hydrostatic.

With the porosities listed in Table 3, groundwater flow paths and pore water velocities were evaluated from all simulations using particle tracking (Pollock, 2016). This enabled us to draw 3 kyr catchment zones for each outlet point (the term 'catchment' is somewhat misleading in this context as no actual recharge takes place). For most scenarios, water particle path lines (blue lines, Fig. 7) depict a multidirectional flow pattern with local catchment zones for each outlet point. A more

395 uniform down-valley-directed flow pattern was simulated for the scenarios with small Q_{REq} and high K (Figs. 7-2a and 7-3a–b). These coincide with partly non-artesian conditions and the lack of discharge at some of the up-valley pingo springs. As also illustrated by the size of the 3 kyr catchment zones, the simulated mean pore water velocities ranged from 0.03 to 0.01 m yr^{-1} (Figs. 7-1a and 7-3c, respectively) and suggest a relatively stagnant groundwater system. This is in accordance with mean residence times that ranged from 70 to 300 kyr (respectively, maximum K and Q_{REq} and minimum K and Q_{REq} scenarios, Figs.

400 7-3c and 7-3a) and by far exceed the duration of the Holocene.

The artesian/non-artesian conditions clearly determine whether outflow takes place at all pingo spring sites, as was indeed the case for all but three simulations (small Q_{REq} and high K, Figs. 7-2a and 7-3a–b). The simulated spring discharge rates (pie charts, Fig. 7) increased with increasing Q_{REq} and decreasing $K,$ and had a maximum value of 0.2 L s^{-1} at FHP for the scenario with maximum Q_{REq} and minimum K (Fig. 7-1c). The simulated proportion of the total outflow discharging to

405 the fjord varied from 42 % to 90 % (the extremes respectively illustrated by Figs. 7-1c and 7-3a). Larger proportions were simulated in the case of high K and a small total inflow Q_{REq}, with the former being the most important parameter.

Figure 7 (next page) Groundwater model simulations from all 9 scenarios. The individual diagrams are sorted so that the hydraulic conductivity increase along the right-hand axis (**1–3**) and the equivalent recharge produced by permafrost aggradation increase along the

410 left-hand axis (**a–c**). On each diagram, the following simulation results are illustrated: Heads from the uppermost grid layer are shown in m a.s.l. by isopotential contours (note that the colour scales are different) and in m a.g.l. by the colour fill. The latter indicates if artesian conditions are simulated (reddish) or not (blueish) (note that **1a–c** each has their own colour scales, whereas the remaining have identical ones). The outflow distribution and discharge rates are illustrated by pie charts with the location of the discharge points (pingos and fjord) indicated on (**1c**). Flow patterns are illustrated by thin blue lines, which each depict pathways of particles released in the uppermost grid

415 layer. The mean pore water velocities, shown in the upper left-hand corners, were calculated from the aforementioned particles and using the same porosities for all scenarios (Table 3). The areas outlined with thick dashed lines show where each outlet point were simulated to receive water from during 3 kyr. In the lower right-hand corner, the simulated head in well DH4 is illustrated on a range plot with the observed head defining the range. The location of DH4 and the pingo springs is marked on (**1c**).

420
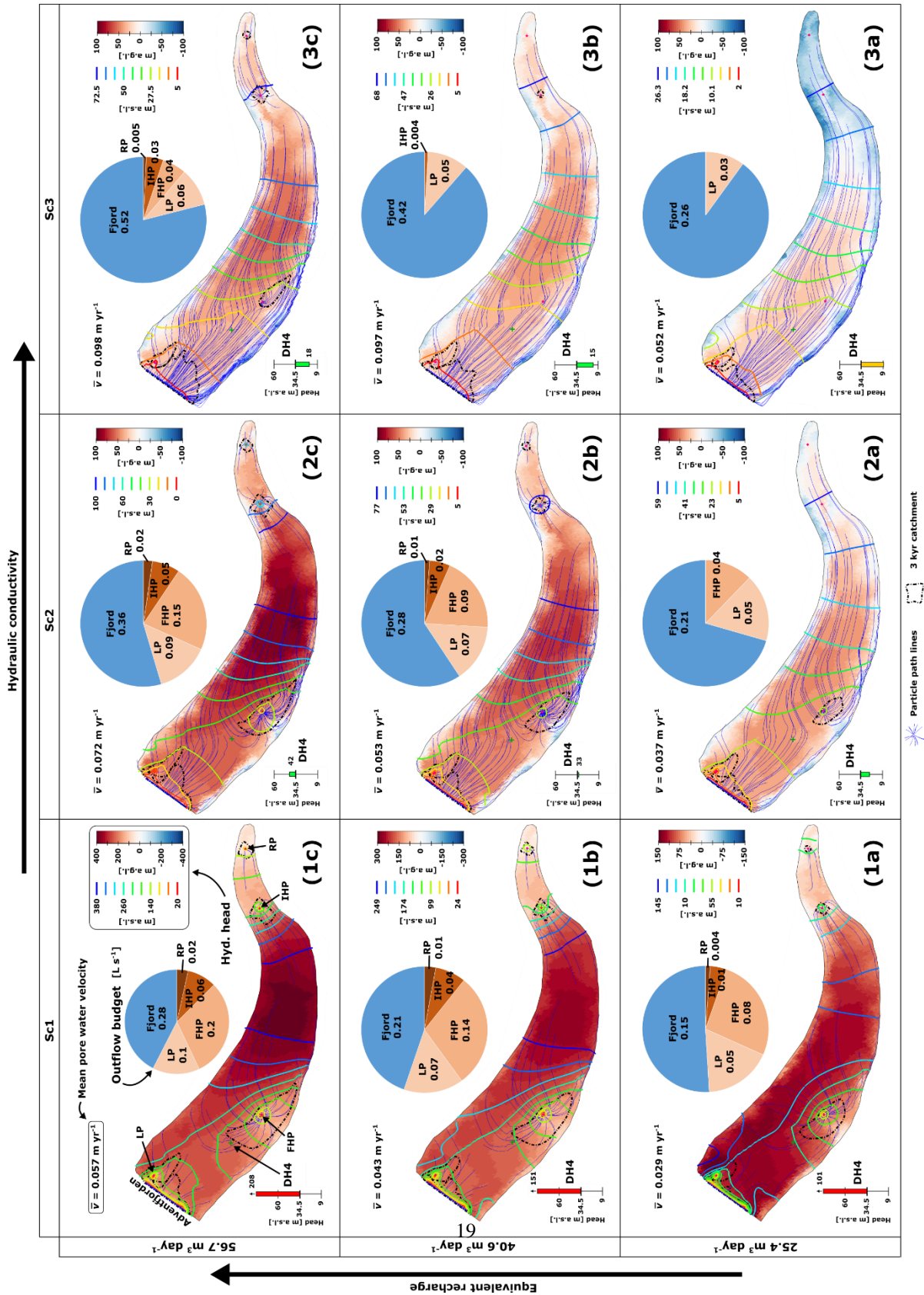
6   Discussion

6.1   Alternative processes producing sub-permafrost overpressures

In this work, we contemplate the implication of deep (sub-permafrost) groundwater systems being restricted from recharge by impervious continuous permafrost. It seems enigmatic that anomalous overpressures and springs still persist in such

425   landscapes, where the lack of warm-based ice at the bottom of glaciers or ice-sheets, or other features capable of maintaining through-taliks as pathways for groundwater flow, seem to rule out recharge from precipitation. Directly supporting the main research hypothesis, the outcomes of our investigation suggest that basal permafrost aggradation due to equilibration of ground temperatures may produce sufficient artesian pressures to sustain such a system. However, other mechanisms producing anomalous pressures relative to hydrostatic conditions cannot be excluded and are therefore considered below.

430   Anomalous pressures may occur in groundwater systems that are either hydrodynamically equilibrated or disequilibrated (Neuzil, 1995). In this context equilibrated means being in steady-state condition with the geological and hydrological setting, while disequilibrated systems are not. For the former, anomalous pressures are typically produced by topography-driven head gradients, but as the permafrost conditions in Adventdalen seem to rule out this process, we focus on the disequilibrium-type of anomalous pressures. These result from geological or glacial processes and can be further classified

435   into systems where anomalous pressures equilibrate to past or ongoing perturbations. Anomalous pressure produced by permafrost aggradation is an example of the latter and we will discuss this in Sect. 6.3 using the model simulation results. In the following, first we consider alternative processes.

6.1.1   Equilibration to past perturbations – glacial loading

A possible interpretation of anomalous overpressure is that a previous perturbation occurred long enough ago to redistribute

440   groundwater (and other fluids) and recently enough for groundwater not to have adjusted to the present conditions (Bahr et al., 1994). The notion of adjustment time becomes convenient when assessing whether an ice-load removed $> 10^4$ yr ago could be responsible for present anomalous pressures. It has been established that the time needed for fluids to redistribute to a pressure perturbation can be expressed by $t_a = l^2 S_s K^{-1}$ (e.g. Neuzil, 2012; Šuklje, 1969), where t_a is the adjustment time, l is half of the shortest dimension of the system, S_s is the specific storage, and K is the hydraulic conductivity. For shallow, low-

445   permeable and well-consolidated bedrock systems like the one investigated in this work, we found t_a to be shorter than the duration of the Holocene. Specifically, we estimated t_a to be between 80 and 7500 years. To quantify this, we used a characteristic length of 200 m. For S_s, we used a matrix compressibility of $7 \cdot 10^{-10}$ to $7 \cdot 10^{-8}$ Pa^{-1} (based on common estimates for fractured rocks, e.g. Domenico and Mifflin, 1965; Domenico and Schwartz, 1998; Fitts, 2002) yielding a S_s of $7 \cdot 10^{-6}$ to $7 \cdot 10^{-4}$ m^{-1} (in line with literature values, c.f. Singhal and Gupta, 2010). For K, we used the lowest estimate of any of the

450   hydrogeological units in question (Table 3) divided by 5 to convert to vertical K. Conclusively, we argue that overpressures in systems like the investigated case cannot be explained by equilibration from past glacial loading.

6.1.2   Equilibration to ongoing perturbations – density contrasts and gases

Past geological or climatic events may be indirectly responsible for ongoing perturbations in systems that adjust to active hydrodynamic processes (Neuzil, 1995). Here, we consider the potential pressure contribution derived from groundwater
455   density contrasts and the occurrence and possible production of gases and gas hydrates.

For a coastal setting like our field site, it is relevant to consider how a potential disequilibrium of the freshwater-saltwater interface could drive groundwater flow. During glaciation, the equilibrium depth of this interface must have been considerably deeper than today if subglacial melting could replenish the groundwater system. Following glacial unloading, the fresh groundwater body is in disequilibrium with the decreased surficial pressure and the density contrast directs hydraulic
460   gradients upwards. Specifically, the freshwater head approximates to 0.025 times the depth of the seawater-freshwater interface, assuming hydrostatic conditions and densities of 1025 and 1000 kg m^{-3} respectively (following the Ghyben-Herzberg relation, Verruijt, 1968). In other terms, to explain artesian pressures resulting in outflow from springs situated at elevations of up to 77 m a.s.l., the seawater-freshwater interface has to be situated at depths down to 3 km b.g.l. unless extensive brine is present. The actual seawater-freshwater interface is most certainly located above this depth, and the observed low-pressures at
465   ~ 800 m b.g.l. (Braathen et al., 2012) definitively exclude density contrasts as a main cause for the overpressures in the shallower system. We conclude that density contrasts may theoretically contribute to the artesian pressures, but only insignificantly.

The presence of gases, either free in solution or bound in gas hydrate complexes (i.e. clathrates), may affect hydraulic pressures (Neuzil, 2003). Pingo spring waters and sub-permafrost groundwater in Adventdalen indeed contain both CH_4 and
470   CO_2 (Hodson et al., In Review). The methane is dominated by a biogenic fingerprint (Hodson et al., 2019) and contemporary methanogenesis is probable (Huq et al., 2017). In order to explain pressure build-up, the essential question is whether any ongoing process produces or releases gas to the groundwater, thereby increasing pressure. Such processes may be exemplified by methanogenesis or clathrate dissolution that causes the partial gas pressure to exceed the hydrostatic pressure, so that free gas forms and replaces groundwater in the pore space. We speculate that, over time, groundwater flow driven by this process
475   is limited, as it represents neither a groundwater source nor a net loss in pore space. In Adventdalen, the pressure and temperature conditions at the base of permafrost are at the threshold for gas hydrate stability, and controlled mainly by the gas composition (Betlem et al., 2019). Whether partly responsible for groundwater flow or not, this proximity to the boundary of hydrate stability means gas clathrates may currently represent a pressure buffer. This is because should clathrates be present, any decrease in pressure to conditions below thermodynamic stability initiates clathrate dissolution, thereby releasing gases
480   and increasing the pressure. It is as yet unclear which form the methane predominantly takes below the permafrost in Adventdalen. However, the near-stability conditions, the documented sub-permafrost gas accumulation and the recent history of climate warming do make the buffering effects of clathrate dissolution more likely.

6.2 Model limitations, extent and uncertainties

For sub-permafrost groundwater systems, an extraordinary amount of relevant data and research exists for Adventdalen (van
der Ploeg et al., 2012) and this arguably makes Adventdalen an optimal case for investigation. There were, nevertheless, too
few observations for calibrating the numerical models in a statistical way, and so in the following, we consider the model
limitations carefully before drawing conclusions from the simulation results.

6.2.1 Limitations related to model approach

Using an approach where transient one-dimensional heat flow modelling was decoupled from steady-state three-
dimensional groundwater modelling required an array of assumptions that deserve attention. Modelling heat transfer one-
dimensionally in the vertical dimension implies that no lateral conduction was considered. The inherent assumption was thus
that the isotherms are horizontally parallel. This assumption holds inland, but for a coastal setting the slope of an isotherm is
expected to increase seawards and in some cases cause a thermal "bulge" under the sea floor (c.f. Gregersen and Eidsmoen,
1988; Taniguchi, 2000). The 1DHT model simulations indicated that even the largest isotherm slope gradients in Adventdalen
are quite small (Fig. 6a). Between the two most seawards points, the gradients for the -2 °C and 0 °C isotherms are -25 and -
35 m km^{-1} ($\Delta z \, \Delta x^{-1}$), respectively, in landwards direction. Effectively, if heat transfer in this work had been modelled in 2D,
the permafrost aggradation rate would have been simulated slightly slower close to the coast due to lateral heat transfer.
Nevertheless, considering how small the isotherm slope gradients are, the lateral heat flow component was considered
negligible and we found the one-dimensional modelling approach appropriate.

The inability to model advective heat transfer represents an uncertainty proportional to the importance of this process
over the time scale in question. From the hydrogeological properties and the spring water chemistry discussed later on, we
realised that the groundwater system must be relatively stagnant. We therefore assumed that the only uncertainty related to the
omission of advective heat transfer arose from neglecting the energy leaving the system with the groundwater. By definition,
the greatest discrepancy between simulations and actual conditions must occur locally at the outflow points to which the
advective heat transfer rate is greatest. On the regional scale, however, we infer that advective heat transfer played an
insignificant role. Disregarding shallow formation of visible ground ice, the total pore water expulsion by freezing
approximates to 9 % of the volume of ice in the pore space. The average pore water velocity of this water when it got expelled
from the system can be approximated by half of the frozen ground depth (assuming this represents the mean travelled distanced)
divided by the porosity and the time it took for frozen ground to establish. For the investigated system this yields a Peclet
number of $P_{e_L} < 0.02$, implying that advective heat transfer played an insignificant role on the regional scale (taking 100 m as
an average frozen ground thickness and characteristic length, and the thermal diffusivity of frozen ground).

The steady-state approach of groundwater modelling implied that dynamic storage effects could not be simulated (S_s,
Eq. 5). In Sect. 6.1.1, we estimated that the groundwater system in Adventdalen has an adjustment time of 80 to 7500 yr. This
suggests that hydraulic pressures can build-up on this time scale. In effect, because of the general decrease of permafrost

515 aggradation rates following the initial formation of frozen ground at ~ 6.5 ka (Fig. 5), the steady-state assumption therefore
likely results in an underestimation of the present-day pressures produced by basal permafrost aggradation.

6.2.2   Model extent uncertainty

Given the lack of known geological boundaries or groundwater divides, the lateral extent of the model domain was defined
using a simplified outline of the HML, but this may be somewhat arbitrary. Due to Early Holocene warming (Fig. 3), the 1DHT
520 simulation results showed that continuous frozen ground in Adventdalen is likely younger than 6.5 ka even where the valley
floor is older (Fig. 5). This is supported by geomorphological and geochronological evidence (Humlum, 2005). As such, there
seems to be no reason why permafrost dynamics outside the HML should be markedly different from that in the up-valley part
of the model area. Based on the above, it is possible that basal permafrost aggradation goes on beyond the model area (HML)
and model simulations may have underestimated the freezing-induced pressures affecting spring discharge.

525   The dominantly low-permeable groundwater system challenged a physically determined lower boundary for the
model domain. From the significant low-pressures observed in deeper stratigraphic layers (~ 800 m b.g.l., Braathen et al.,
2012), we inferred isolation of the investigated groundwater system from that below and simply assigned the base to a depth
of 300 m b.g.l. By simulating scenarios with a lower base of 250 and 400 m b.g.l., we found that simulation results did not
change significantly (< 1 % deviation of simulated heads and discharge rates).

530 **6.3   Do model simulations represent the processes in the groundwater system in Adventdalen?**

The amount of hydrogeological data from Adventdalen was insufficient for automatic calibration of model parameters.
However, some scenarios yielded simulations that must be considered at odds with the available observations. For the low K
scenarios (Figs. 7-1a–c), the simulated hydraulic heads were almost certainly too high. The only head observation supports
this view and we therefore suggest that the real hydraulic conductivities must be greater than those employed here. Further,
535 discharge from all of the observed pingo springs was not simulated for scenarios with high K's and low equivalent recharge.
This could indicate that the real K-values are in effect lower than those employed for these scenarios. However, since dynamic
storage effects and alternative processes contributing to hydraulic pressure were not incorporated in the model, these high K
scenarios are almost certainly wrong. Therefore, the most plausible representation of the system is likely to be found within
the scenarios shown in Figs. 7-2b–c and 7-3c).

540   For the flow pattern, a more certain conclusion could be drawn. The flow was simulated to be multidirectional, with
local sub-catchments appearing whenever the groundwater model was able to simulate artesian spring discharges from the
pingos. This indicates that regional groundwater flow across the model area is very limited.

On Fig. 8, simulated spring outflows from all model simulations are plotted together with the few available
observations. Validation of any particular model scenario was not possible due to the variability and paucity of observations.
545 Nevertheless, assuming that only a small fraction of the discharge (if any) freezes within the pingo and becomes part of its
core, the comparable observed and simulated discharges suggest that permafrost aggradation alone can explain the presence

of the pingos and their springs in a low-permeability system like Adventdalen. To investigate the effect of additional pressure sources, we ran the groundwater model with maximum K values (Table 3) and different, uniformly distributed recharge rates, all resulting in a greater total inflow of groundwater than from permafrost aggradation alone (Fig. 7). Figure 9 illustrates such

550   a scenario with a recharge rate of 1 mm yr^{-1}. We found that, if the pressure production exceeds that equivalent to a recharge rate of 1 mm yr^{-1}, hydraulic heads rise unrealistically (i.e. > 200 m a.g.l.). Within the model limitations (Sect. 6.2), Fig. 9 may thus be regarded as an approximation of the upper limit of possible total inflow (or pore space loss) rates (161.4 m^3 day^{-1}). The corresponding spring water discharge rates range from 0.11 to 0.46 L s^{-1} (Fig. 8) and the mean residence time is 24 kyr.
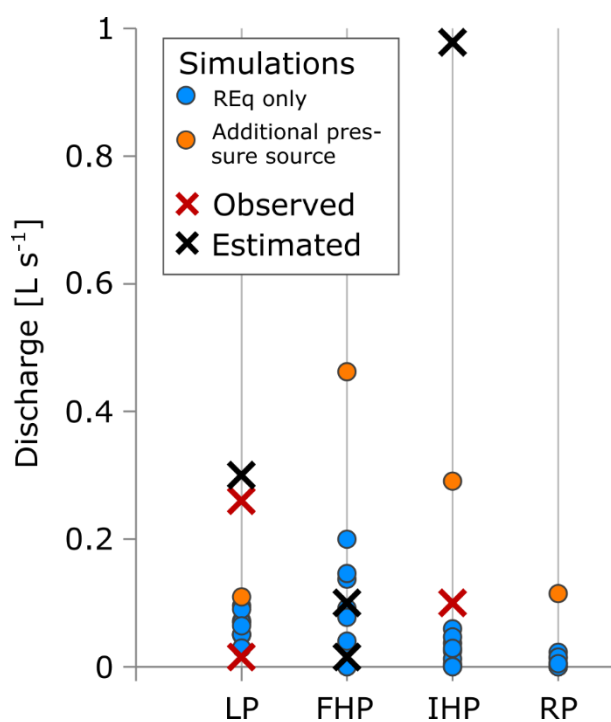
555

Figure 8 Simulated, observed (measured) and estimated ("by the eye") spring discharge rates. Blue dots are discharge rates simulated for groundwater model scenarios where the source term is defined by the rate of basal permafrost aggradation (Figs. 6 and 7). The orange dots are discharge rates simulated for a groundwater scenario with an additional unknown pressure source (Fig. 9).
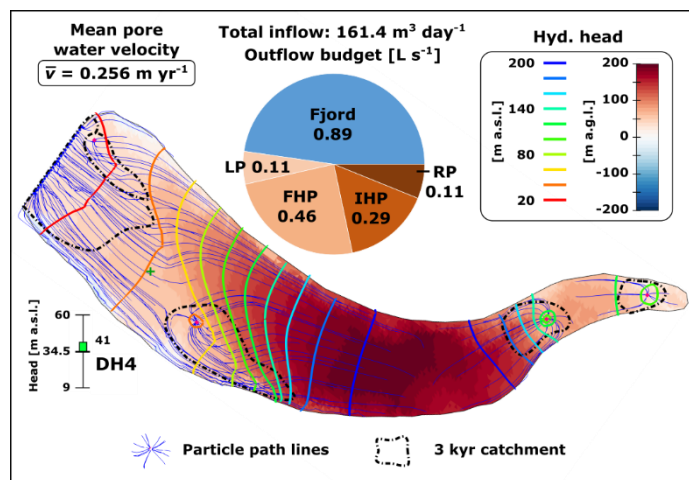
Figure 9 Groundwater model simulation representing additional pressure sources. Recharge is distributed uniformly with a rate of 1 mm yr⁻¹.

6.4 Comparison with hydrological processes inferred from pingo spring water chemistry

The lack of data for model calibration and other shortcomings related to our model approach posed challenges for conclusive interpretations based on the modelling results alone. However, hydrochemical data from 25 pingo spring water samples from 2014 to 2017 presented by Hodson et al. (In Review) and publicly available from DOI:10.5285/3d82fd3f-884b-47b6-b11c-6c96d66b950d give additional insights into the groundwater system. Water samples from LP, FHP, IHP and RP reveal that all these pingo springs share the same sodium-bicarbonate ($NaHCO_3$) water type (illustrated in the Supplement), which is commonly associated with freshening of a saline groundwater system (e.g. Giménez-Forcada, 2010). The only exceptions are four samples taken near River Pingo in 2017 of a magnesium-sulfate water type. These four samples were excluded from the following discussion because they might not be associated with a pingo according to Hodson et al. (In Review).

Among the 21 $NaHCO_3$-dominated samples a few distinct trends were observed in the hydrochemistry. Specifically, the concentration of Cl^- and heavy stable water isotopes both increase in the up-valley direction. To illustrate this, the concentration of Cl^- is plotted against $\delta^{18}O_{H_2O}$ in Fig. 10. The former has a relatively constant concentration at each site compared to the latter. We inferred that the variation of the Cl^- concentrations between the different springs reflects an up-valley variation in the sub-permafrost groundwater system, and not processes acting locally along the flow paths towards the individual pingos. If the latter had been the case, we would expect to see greater intra-site variation.

In order to explain the increasing Cl^- concentration and $\delta^{18}O_{H_2O}$ we considered solute rejection and isotope fractionation associated with freezing as well as mixing between seawater and freshwater. For the former, we found that the positive relationship between the two parameters was incongruent with this being a major control in the investigated system: when ice forms, water molecules containing the heavier isotope ^{18}O (and D) are preferentially included in the ice, while the

residual water becomes isotopically lighter. For freezing in a well-mixed and closed reservoir, the isotopic ratio in the residual water, δ_w, may be expressed by a Rayleigh-type fractionation according to the following equation (Lacelle, 2011):

$$\delta_w = \delta_0 + \ln(\alpha_{i-w}) \cdot 1000 \cdot \ln(f) \qquad (8)$$

where δ_0 is the initial isotopic ratio in the water, α_{i-w} is the fractionation coefficient between ice and water, and f is the

585   fraction of residual water. $\alpha_{i-w} = 1.003$ (Lehmann and Siegenthaler, 1991) at equilibrium and approaches 1 for faster freezing rates (non-equilibrium). The decrease of $\delta^{18}O_{H_2O}$ in the residual water resulting from freezing is exemplified on Fig. 10 by taking a typical LP water sample (i.e. with the lowest salinity) and assuming that Cl$^-$ is completely excluded from the ice. The shading indicates the possible range of $\delta^{18}O_{H_2O}$ that can be derived from this process. Although two samples from FHP fall within the shaded area, it was hard to explain the composition of these with freezing from a LP-type water, as the remaining

590   samples did not comply with this interpretation (Fig. 10).

Another model line on Fig. 10 is drawn by assuming that the LP samples result from mixing of seawater and a freshwater end-member with zero Cl$^-$ concentration. Generally, the remaining samples agree with this model line and hence we argue that mixing is the more feasible explanation. This was also in line with the interpretation that the NaHCO$_3$-dominated hydrochemistry reflects freshening.

595
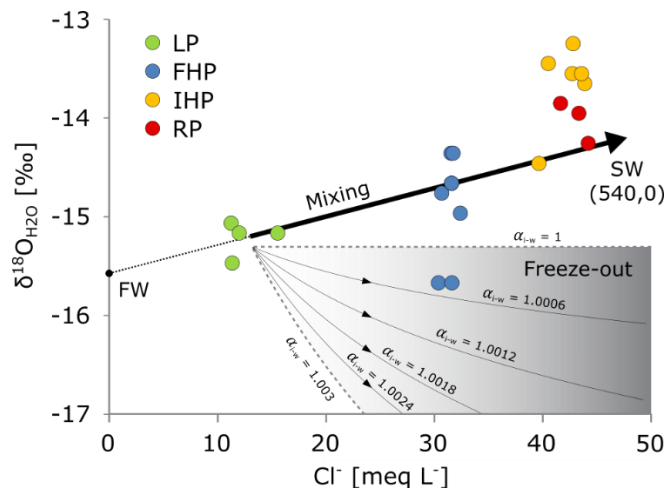
Figure 10 Cl$^-$ concentration and $\delta^{18}O_{H_2O}$ of pingo spring water samples. The thick black model line is drawn by assuming that the LP samples result from mixing of seawater and a freshwater endmember with a zero Cl$^-$ concentration. The range of possible $\delta^{18}O_{H_2O}$ values following freeze-out (Eq. 8) from water with an initial composition alike LP is illustrated with the shaded area. Here, Cl$^-$ is assumed to be

600   completely excluded from the ice. The lower and upper edges of the shading represent equilibrium fractionation and no fractionation, respectively, while the intermediate model lines illustrate fractionation at 20 %, 40 %, 60 % and 80 % (top–down) of equilibrium conditions.

For the above mixing scenario, field surveys suggested a somewhat unusual trend with greater fractions of freshwater towards the sea, where $\delta^{18}O_{H_2O}$ and Cl$^-$ concentrations approach those of the inferred freshwater end-member in Fig. 10. In

605   the case of present-day recharge from the adjacent mountains (as demonstrated at a pingo 35 km South West of Adventdalen

by Demidov et al., 2019), we would not expect to observe such a systematic trend along the valley axis, as this would be unlikely in a system dependent upon localised areas for infiltration. We therefore suggest that the unexpected landwards increase in Cl⁻ is difficult to explain without the sequence of events illustrated in Fig. 11. During glaciation, the groundwater system was recharged by subglacial melting (Fig. 11a). Despite being covered by the sea during the Early Holocene, seawater

610   could not infiltrate substantially into the groundwater system to replace the fresh groundwater (Fig. 11b). On Fig. 11c, the body of freshwater forms a wedge that thins inland below the freezing front due to the density difference with seawater. Moving away from the sea, the springs expel more saline groundwater because the wedge thins in this direction and the permafrost thickness increases (Fig. 11c). Therefore both the sources of water and the hydraulic conditions of the groundwater system seem intricately linked to landscape evolution throughout the Holocene.

615
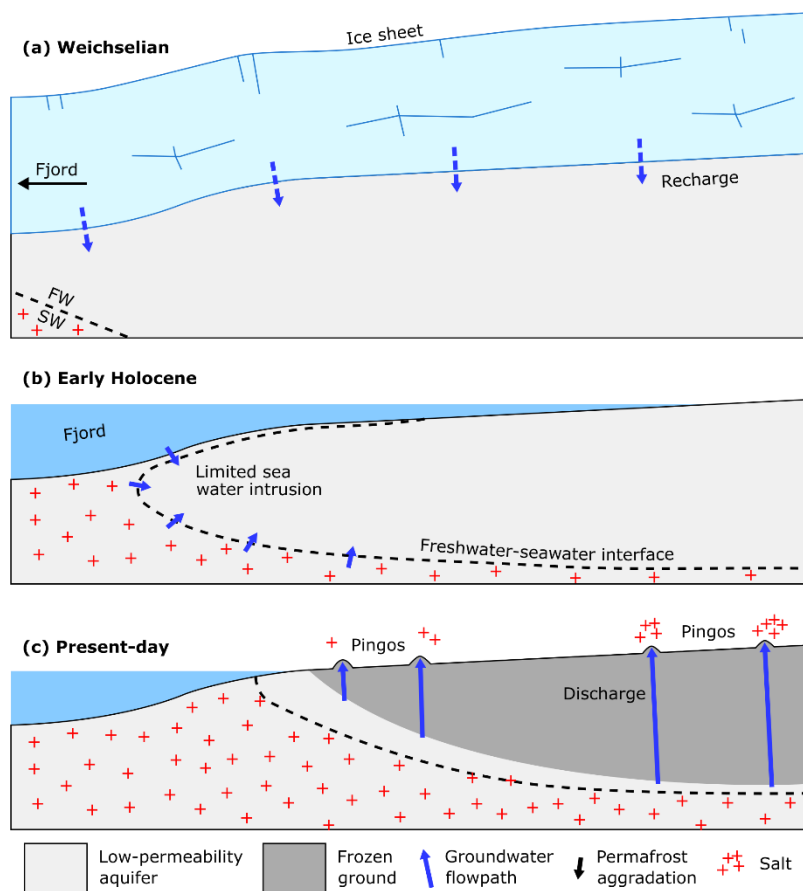
Figure 11 Possible interpretation of hydrochemical trends observed in pingo spring waters. **(a)** Subglacial melting from the Weichselian ice sheet recharged the groundwater system with freshwater. **(b)** Although covered by the sea during Early Holocene, low-permeability rocks limited infiltration of sea water and the fresh groundwater body persisted. **(c)** Due to the shallower permafrost depth towards the sea, spring

620   water sampled in this direction holds a lower concentration of sea water (salt).

7   Conclusions

Results from the decoupled heat and groundwater model show that millennial-scale basal permafrost aggradation may alone produce hydraulic pressures sufficient for the formation of pingos and their spring water outflows. In addition to the climate cooling necessary for permafrost aggradation, a relatively low-permeability groundwater system with limited dissipation of
625 hydraulic pressures are also required for pingo formation. Pingos formed in this way do not conform to the traditional differentiation between open-system and closed-system types, but constitute a borderline case: by definition, they classify as open-system pingos, because the groundwater body from which spring water is expelled is not enclosed in permafrost. Generically though, they relate more to closed-system pingos, because the causal mechanism of hydraulic pressures is essentially similar, although operating over much longer time-scales. We emphasise that this conceptual model for pingo
630 formation represents an end-member of pingo-forming processes, which is not exclusive, but may act in combination with others, such as those reported nearby by Demidov et al. (2019).

        The simulation results from the 1DHT model suggested that basal permafrost aggradation in Adventdalen presently induces head gradients corresponding to the effect of a recharge rate of ~ 0.1 mm yr^{-1} furthest up-valley, and increasing to ~ 1 mm yr^{-1} towards the sea. By applying these rates to the groundwater model, we simulated spring outflow rates of the order of
635 10^{-1} L s^{-1}. Due to the omission of dynamic storage effects (i.e. a steady-state assumption), and to the probable occurrence of basal permafrost aggradation outside the model area, these are likely to be underestimations. Nevertheless, the simulated and observed spring outflow rates at Adventdalen pingos were of the same order of magnitude, suggesting that they likely form in accordance with our conceptual model that is driven by basal permafrost aggradation. This further suggests that overpressures in other sub-permafrost groundwater systems can result from permafrost aggradation.

640   The simulated aquifer flow paths and flow velocity distributions suggested that sub-permafrost groundwater flow in Adventdalen is characterised by slow mean pore water velocities (<0.25 m yr^{-1}) and long residence times (> 2.5·10^4 yr) that exceed the duration of the Holocene. The groundwater system most likely has a multidirectional flow pattern with individual catchments around each pingo.

        The presence of a positive relationship between Cl$^-$ and $\delta^{18}O_{H_2O}$ in the pingo spring water samples suggests that
645 mixing between seawater and freshwater is the major control of hydrogeochemistry in the sub-permafrost groundwater system prior to aggradation. As a result, a somewhat unusual but clear trend of increasing salinity in an up-valley direction was found. Therefore, given the relatively stagnant groundwater system, Weichselian subglacial meltwater could endure the Early Holocene inundation and result in the present-day situation where a freshwater body forms a wedge that thins in the inland direction below the permafrost. This possible interpretation readily explains the inland increase of the spring salinity because
650 the inland springs expel groundwater from greater and hence more saline depths.

        Alternative and non-recharge-related processes that may also affect sub-permafrost pressures were considered. The role of gases may be particularly important in this context because it is likely that methane hydrates have influenced the groundwater system under investigation. However, methane hydrate dissolution may in fact act as a pressure buffer and prolong

artesian pressures after permafrost ceases aggrading (or starts thawing). This represents an uncertainty in forecasting how
655 groundwater and methane fluxes will react to climate change. Unresolved questions regarding the occurrence and formation
of gases in sub-permafrost groundwater systems therefore constitute an ongoing challenge for Arctic science.

8 Code availability

The 1DHT model code is publicly available at DOI:10.5281/zenodo.3578839.

Author contributions

660 MTH developed the 1DHT model code and designed the modelling experiments with contributions from VB. AJH, SJ and
MTH analysed the hydrochemical data. MTH prepared the manuscript with contributions from all the co-authors.

Competing financial interest

The authors declare no competing financial interests.

Acknowledgements

665 This paper largely emanated from work initiated with MTH's MSc thesis (Hornum, 2018) and the authors acknowledge Prof.
Peter Engesgaard for supervising the thesis work. The authors also acknowledge The Research Council of Norway grant
294764.

References

Åhman, R.: Studier av pingoer i Adventdalen och Reindalen på Spetsbergen, Lunds Univ. Naturgeografiska Institution. Rapp.
670 och Not., 15, 27–44, 1973.

Andersen, D. T., Pollard, W. H., McKay, C. P. and Heldmann, J.: Cold springs in permafrost on Earth and Mars, J. Geophys.
Res. E Planets, 107(3), doi:10.1029/2000je001436, 2002.

AQUAVEO™: Groundwater Modeling System 10.4.4, [online] Available from: https://www.aquaveo.com/software/gms-
groundwater-modeling-system-introduction, 2019.

675 Bælum, K., Johansen, T. A., Johnsen, H., Rød, K., Ruud, B. O. and Braathen, A.: Subsurface structures of the longyearbyen
CO2 lab study area in central spitsbergen (arctic Norway), as mapped by reflection seismic data, Nor. Geol. Tidsskr., 92(4),
377–389, 2012.

Bahr, J. M., Moline, G. R. and Nadon, G. C.: Anomalous Pressures in the Deep Michigan Basin, in AAPG Memoir 61: Basin Compartmensts and Seals, pp. 153–165., 1994.

680   Ballantyne, C. K.: Periglacial geomorphology, 1st ed., Wiley-Blackwell., 2018.

Benn, D. I. and Evans, D. J. A.: Glaciers & Glaciation, 2nd ed., Hodder Education., 2010.

Bense, V. F., Kooi, H., Ferguson, G. and Read, T.: Permafrost degradation as a control on hydrogeological regime shifts in a warming climate, J. Geophys. Res. Earth Surf., 117(3), 1–18, doi:10.1029/2011JF002143, 2012.

Bergman, T. L., Lavine, A. S., Incropera, F. P. and Dewitt, D. P.: Fundamentals of Heat and Mass Transfer, 7th ed., John
685   Wiley & Sons., 2011.

Betlem, P., Senger, K. and Hodson, A.: 3D thermobaric modelling of the gas hydrate stability zone onshore central Spitsbergen, Arctic Norway, Mar. Pet. Geol., 100(August 2018), 246–262, doi:10.1016/j.marpetgeo.2018.10.050, 2019.

van der Bilt, W. G. M., D'Andrea, W. J., Bakke, J., Balascio, N. L., Werner, J. P., Gjerde, M. and Bradley, R. S.: Alkenone-based reconstructions reveal four-phase Holocene temperature evolution for High Arctic Svalbard, Quat. Sci. Rev., 183, 204–
690   213, doi:10.1016/j.quascirev.2016.10.006, 2018.

Birchall, T., Senger, K., Hornum, M. T., Olaussen, S. and Braathen, A.: Underpressure of the Northern Barents Shelf: distribution, causes and implications on the petroleum. In Review, Am. Assoc. Pet. Geol. Bull., n.d.

Bonacina, C. and Comini, G.: On the solution of the nonlinear heat conduction equations by numerical methods, Int. J. Heat Mass Transf., 16(3), 581–589, doi:10.1016/0017-9310(73)90225-1, 1973.

695   Braathen, A., Bælum, K., Christiansen, H. H., Dahl, T., Eiken, O., Elvebakk, H., Hansen, F., Hanssen, T. H., Jochmann, M., Johansen, T. A., Johnsen, H., Larsen, L., Lie, T., Mertes, J., Mørk, A., Mørk, M. B., Nemec, W., Olaussen, S., Oye, V., Rød, K., Titlestad, G. O., Tveranger, J. and Vagle, K.: The Longyearbyen CO2 Lab of Svalbard, Norway - Initial Assessment of the Geological Conditions for CO2 Sequestration, Nor. Geol. Tidsskr., 92(4), 353–376, 2012.

Burr, D. M., Tanaka, K. L. and Yoshikawa, K.: Pingos on Earth and Mars, Planet. Space Sci., 57(5–6), 541–555,
700   doi:10.1016/j.pss.2008.11.003, 2009.

Burt, T. P. and Williams, P. J.: Hydraulic conductivity in frozen soils, Earth Surf. Process., 1(4), 349–360, doi:10.1002/esp.3290010404, 1976.

Cable, S., Elberling, B. and Kroon, A.: Holocene permafrost history and cryostratigraphy in the High-Arctic Adventdalen Valley, central Svalbard, Boreas, 47(2), 423–442, doi:10.1111/bor.12286, 2018.

705   Carslaw, H. S. and Jaeger, J. C.: Conduction of heat in solids, 2nd ed., Clarendon Press., 1959.

Christiansen, H. H., French, H. M. and Humlum, O.: Permafrost in the Gruve-7 mine, Adventdalen, Svalbard, Nor. Geogr.

Tidsskr., 59(2), 109–115, doi:10.1080/00291950510020592, 2005.

Demidov, N., Wetterich, S., Verkulich, S., Ekaykin, A., Meyer, H., Anisimov, M., Schirrmeister, L., Demidov, V. and Hodson, A. J.: Geochemical signatures of pingo ice and its origin in Grøndalen, west Spitsbergen, Cryosph., 13(11), 3155–3169, doi:10.5194/tc-13-3155-2019, 2019.

710 Domenico, P. A. and Mifflin, M. D.: Water from low-permeability sediments and land subsidence, Water Resour. Res., 1(4), 563–576, doi:10.1029/WR001i004p00563, 1965.

Domenico, P. A. and Schwartz, F. W.: Physical and chemical hydrogeology, Wiley & Sons., 1998.

Dyke, A. S., England, J., Reimnitz, E. and Jette, H.: Changes in driftwood delivery to the Canadian Arctic Archipelago, Arctic, 50(1), 1–16, 1997.

715 Elverhøi, A., Svendsen, J. I., Solheim, A., Andersen, E. S., Milliman, J., Mangerud, J. and Hooke, R. L.: Late Quaternary Sediment Yield from the High Arctic Svalbard Area, J. Geol., 103(1), 1–17, doi:10.1086/629718, 1995.

Eppelbaum, L., Kutasov, I. and Pilchin, A.: Applied Geothermics, Lect. Notes Earth Syst. Sci., 757, doi:10.1007/978-3-642-34023-9, 2014.

720 Farnsworth, W.: Holocene glacier history of Svalbard: Retracing the style of (de-)glaciation, UiT The Arctic University of Norway., 2019.

Farouki, O. T.: Thermal Properties of Soils - CRREL Monograph, US Army Cold Reg. Res. Eng. Lab., 1981.

Fitts, C. R.: Groundwater Science, 1st ed., Academic Press., 2002.

Førland, E. J., Hanssen-Bauer, I. and Nordli, Ø.: Climate statistics and longterm series of temperature and precipitation at 725 Svalbard and Jan Mayen, Norwegian Meteorological Institute, DNMI Nor. Meteorol. Inst. Rep., 21, 1997.

Forman, S. L.: Post-glacial relative sea-level history of northwestern Spitsbergen, Svalbard, Geol. Soc. Am. Bull., 102(11), 1580–1590, doi:10.1130/0016-7606(1990)102<1580:PGRSLH>2.3.CO;2, 1990.

Forwick, M. and Vorren, T. O.: Stratigraphy and deglaciation of the Isfjorden area, Spitsbergen, Nor. Geol. Tidsskr., 90(4), 163–179, 2011.

730 French, H. M.: The Periglacial Environment, 4th ed., John Wiley & Sons Ltd., 2017.

Funder, S., Goosse, H., Jepsen, H., Kaas, E., Kjær, K. H., Korsgaard, N. J., Larsen, N. K., Linderson, H., Lyså, A., Möller, P., Olsen, J. and Willerslev, E.: A 10,000-year record of Arctic Ocean Sea-ice variability - View from the beach, Science (80-.)., 333(6043), 747–750, doi:10.1126/science.1202760, 2011.

Gilbert, G. L., O'Neill, H. B., Nemec, W., Thiel, C., Christiansen, H. H. and Buylaert, J. P.: Late Quaternary sedimentation 735 and permafrost development in a Svalbard fjord-valley, Norwegian high Arctic, Sedimentology, 65(7), 2531–2558,

doi:10.1111/sed.12476, 2018.

Giménez-Forcada, E.: Dynamic of sea water interface using hydrochemical facies evolution diagram, Ground Water, 48(2), 212–216, doi:10.1111/j.1745-6584.2009.00649.x, 2010.

Govaerts, J., Beerten, K. and Ten Veen, J.: Weichselian permafrost depth in the Netherlands: A comprehensive uncertainty
740 and sensitivity analysis, Cryosphere, 10(6), 2907–2922, doi:10.5194/tc-10-2907-2016, 2016.

Grasby, S. E., Beauchamp, B. and Bense, V.: Sulfuric acid speleogenesis associated with a glacially driven groundwater system-paleo-spring "pipes" at Borup Fiord Pass, Nunavut, Astrobiology, 12(1), 19–28, doi:10.1089/ast.2011.0700, 2012.

Grasby, S. E., Proemse, B. C. and Beauchamp, B.: Deep groundwater circulation through the High Arctic cryosphere forms Mars-like gullies, Geology, 42(8), 651–654, doi:10.1130/G35599.1, 2014.

745 Gregersen, O. and Eidsmoen, T.: Permafrost conditions in the shore area at Svalbard, in Permafrost, proceedings of the Fifth International Conference on Permafrost, August 2-5, 1988, Trondheim, Norway, vol. 2, edited by K. Senneset, pp. 933–936, Tapir Publishers., 1988.

Grenier, C., Anbergen, H., Bense, V., Chanzy, Q., Coon, E., Collier, N., Costard, F., Ferry, M., Frampton, A., Frederick, J., Gonçalvès, J., Holmén, J., Jost, A., Kokh, S., Kurylyk, B., McKenzie, J., Molson, J., Mouche, E., Orgogozo, L., Pannetier, R.,
750 Rivière, A., Roux, N., Rühaak, W., Scheidegger, J., Selroos, J. O., Therrien, R., Vidstrand, P. and Voss, C.: Groundwater flow and heat transport for systems undergoing freeze-thaw: Intercomparison of numerical simulators for 2D test cases, Adv. Water Resour., 114(February), 196–218, doi:10.1016/j.advwatres.2018.02.001, 2018.

Grosse, G., Goetz, S., McGuire, A. D., Romanovsky, V. E. and Schuur, E. A. G.: Changing permafrost in a warming world and feedbacks to the Earth system, Environ. Res. Lett., 11, 040201, doi:10.1088/1748-9326/11/4/040201, 2016.

755 Grundvåg, S.-A., Jelby, M. E., Sliwinska, K. K., Nøhr-Hansen, H., Aadland, T., Sandvik, S. E., Tennvassås, I., Engen, T. and Olaussen, S.: Sedimentology and palynology of the Lower Cretaceous succession of central Spitsbergen: integration of subsurface and outcrop data, Nor. J. Geol., 99(2), doi:10.17850/njg006, 2019.

Hald, M., Andersson, C., Ebbesen, H., Jansen, E., Klitgaard-Kristensen, D., Risebrobakken, B., Salomonsen, G. R., Sarnthein, M., Sejrup, H. P. and Telford, R. J.: Variations in temperature and extent of Atlantic Water in the northern North Atlantic
760 during the Holocene, Quat. Sci. Rev., 26, 3423–3440, doi:10.1016/j.quascirev.2007.10.005, 2007.

Haldorsen, S., Heim, M. and Lauritzen, S. E.: Subpermafrost Groundwater, Western Svalbard, Nord. Hydrol., 27(1–2), 57–68, doi:10.2166/nh.1996.0019, 1996.

Hanssen-Bauer, I., Førland, E. J., Hisdal, H., Mayer, S., Sandø, A. B., Sorteberg, A., Adakudlu, M., Andresen, J., Bakke, J., Beldring, S., Benestad, R., Bilt, W., Bogen, J., Borstad, C., Breili, K., Breivik, Ø., Børsheim, K. Y., Christiansen, H. H.,
765 Dobler, A., Engeset, R., Frauenfelder, R., Gerland, S., Gjelten, H. M., Gundersen, J., Isaksen, K., Jaedicke, C., Kierulf, H.,

Kohler, J., Li, H., Lutz, J., Melvold, K., Mezghani, A., Nilsen, F., Nilsen, I. B., Nilsen, J. E. Ø., Pavlova, O., Ravndal, O., Risebrobakken, B., Saloranta, T., Sandven, S., Schuler, T. V, Simpson, M. J. R., Skogen, M., Smedsrud, L. H., Sund, M., Vikhamar-Schuler, D., Westermann, S. and Wong, W. K.: Climate in Svalbard 2100. [online] Available from: http://www.miljodirektoratet.no/M1242 (Accessed 12 September 2019), 2018.

770   Hodson, A., Nowak, A., Senger, K., Redeker, K. R., Christiansen, H. H., Jessen, S., Hornum, M. T., Betlem, P., Thornton, S., Turchyn, A. V., Olaussen, S. and Marca, A.: Open system pingos as hotspots for sub-permafrost methane emission in Svalbard, Cryosph. Discuss., doi:10.5194/tc-2020-11, in review, 2020.

Hodson, A. J., Nowak, A., Redeker, K. R., Holmlund, E. S., Christiansen, H. H. and Turchyn, A. V.: Seasonal dynamics of methane and carbon dioxide evasion from an open system pingo: Lagoon pingo, svalbard, Front. Earth Sci., 7, 30,
775   doi:10.3389/feart.2019.00030, 2019.

Hornum, M. T.: Postglacial Rebound, Permafrost Growth, and its Impact on Groundwater Flow and Pingo Formation, University of Copenhagen. [online] Available from: https://www.researchgate.net/profile/Mikkel_Hornum2, 2018.

Humlum, O.: Holocene permafrost aggradation in Svalbard, Geol. Soc. Spec. Publ., 242, 119–130, doi:10.1144/GSL.SP.2005.242.01.11, 2005.

780   Humlum, O., Instanes, A. and Sollid, J. L.: Permafrost in Svalbard: A review of research history, climatic background and engineering challenges, Polar Res., 22(2), 191–215, doi:10.3402/polar.v22i2.6455, 2003.

Huq, F., Smalley, P. C., Mørkved, P. T., Johansen, I., Yarushina, V. and Johansen, H.: The Longyearbyen CO2 Lab: Fluid communication in reservoir and caprock, Int. J. Greenh. Gas Control, doi:10.1016/j.ijggc.2017.05.005, 2017.

Ingólfsson, Ó. and Landvik, J. Y.: The Svalbard-Barents Sea ice-sheet-Historical, current and future perspectives, Quat. Sci.
785   Rev., 64, 33–60, doi:10.1016/j.quascirev.2012.11.034, 2013.

Koevoets, M. J., Hammer, Ø., Olaussen, S., Senger, K. and Smelror, M.: Integrating subsurface and outcrop data of the Middle Jurassic to Lower Cretaceous Agardhfjellet Formation in central Spitsbergen, Nor. J. Geol., 98(4), doi:10.17850/njg98-4-01, 2018.

Kottek, M., Grieser, J., Beck, C., Rudolf, B. and Rubel, F.: World Map of the Köppen-Geiger climate classification updated, ,
790   15(3), 259–263, doi:10.1127/0941-2948/2006/0130, 2006.

Lacelle, D.: On the δ18O, δD and D-excess relations in meteoric precipitation and during equilibrium freezing: Theoretical approach and field examples, Permafr. Periglac. Process., 22(1), 13–25, doi:10.1002/ppp.712, 2011.

Lehmann, M. and Siegenthaler, U.: Equilibrium oxygen- and hydrogen-isotope fractionation between ice and water, J. Glaciol., 37(125), 23–26, doi:10.3189/s0022143000042751, 1991.

795   Liestøl, O.: Pingos, springs, and permafrost in Spitsbergen, Nor. Polarinstitutt Årb. 1975, 7–29, 1977.

Liestøl, O.: Open-system pingos in Spitsbergen, Nor. Geogr. Tidsskr., doi:10.1080/00291959608552355, 1996.

Lønne, I. and Nemec, W.: High-arctic fan delta recording deglaciation and environment disequilibrium, Sedimentology, 51(3), 553–589, doi:10.1111/j.1365-3091.2004.00636.x, 2004.

Mackay, J. R.: Pingo growth and collapse, Tuktoyaktuk Peninsula area, western arctic coast, Canada: A long-term field study, Geogr. Phys. Quat., 52(3), 271–323, doi:10.7202/004847ar, 1998.

Manger, G. E.: Porosity and Bulk Density of Sedimentary Rocks, Geol. Surv. Bull., 1144-E, doi:10.1111/nan.12452, 1963.

Mangerud, J. and Svendsen, J. I.: The Holocene Thermal Maximum around Svalbard, Arctic North Atlantic; molluscs show early and exceptional warmth, The Holocene, 28(1), 65–83, doi:10.1177/0959683617715701, 2017.

MathWorks®: MATLAB R2019b, [online] Available from: https://se.mathworks.com/products/matlab.html, 2019.

Mau, S., Römer, M., Torres, M. E., Bussmann, I., Pape, T., Damm, E., Geprägs, P., Wintersteller, P., Hsu, C. W., Loher, M. and Bohrmann, G.: Widespread methane seepage along the continental margin off Svalbard-from Bjørnøya to Kongsfjorden, Sci. Rep., 7, doi:10.1038/srep42997, 2017.

McCauley, C. A., White, D. M., Lilly, M. R. and Nyman, D. M.: A comparison of hydraulic conductivities, permeabilities and infiltration rates in frozen and unfrozen soils, Cold Reg. Sci. Technol., 34(2), 117–125, doi:10.1016/S0165-232X(01)00064-7, 2002.

McDonald, M. G. and Harbaugh, A. W.: A modular three-dimensional finite-difference ground-water flow model - Techniques of Water-Resources Investigations 06-A1., 1988.

Mottaghy, D. and Rath, V.: Latent heat effects in subsurface heat transport modelling and their impact on palaeotemperature reconstructions, Geophys. J. Int., 164(1), 236–245, doi:10.1111/j.1365-246X.2005.02843.x, 2006.

Myhre, C. L., Ferré, B., Platt, S. M., Silyakova, A., Hermansen, O., Allen, G., Pisso, I., Schmidbauer, N., Stohl, A., Pitt, J., Jansson, P., Greinert, J., Percival, C., Fjaeraa, A. M., O'Shea, S. J., Gallagher, M., Le Breton, M., Bower, K. N., Bauguitte, S. J. B., Dalsøren, S., Vadakkepuliyambatta, S., Fisher, R. E., Nisbet, E. G., Lowry, D., Myhre, G., Pyle, J. A., Cain, M. and Mienert, J.: Extensive release of methane from Arctic seabed west of Svalbard during summer 2014 does not influence the atmosphere, Geophys. Res. Lett., 43(9), 4624–4631, doi:10.1002/2016GL068999, 2016.

Neuzil, C. E.: Abnormal pressures as hydrodynamic phenomena, Am. J. Sci., 295(6), 742–786, doi:10.2475/ajs.295.6.742, 1995.

Neuzil, C. E.: Hydromechanical coupling in geologic processes, Hydrogeol. J., 11(1), 41–83, doi:10.1007/s10040-002-0230-8, 2003.

Neuzil, C. E.: Hydromechanical effects of continental glaciation on groundwater systems, Geofluids, 12(1), 22–37,

825   doi:10.1111/j.1468-8123.2011.00347.x, 2012.

Nordli, Ø., Przybylak, R., Ogilvie, A. E. J. and Isaksen, K.: Long-term temperature trends and variability on spitsbergen: The extended svalbard airport temperature series, 1898-2012, Polar Res., 33(1), 21349, doi:10.3402/polar.v33.21349, 2014.

Norwegian Polar Institute: Map data, [online] Available from: https://geodata.npolar.no/ (Accessed 13 September 2019), 2019.

Ohm, S. E., Larsen, L., Olaussen, S., Senger, K., Birchall, T., Demchuk, T., Hodson, A., Johansen, I., Titlestad, G. O., Karlsen,
830   D. A. and Braathen, A.: Discovery of shale gas in organic-rich Jurassic successions, Adventdalen, Central Spitsbergen, Norway, Nor. J. Geol., 99(2), 1–28, doi:10.17850/njg007, 2019.

Olaussen, S., Senger, K., Braathen, A., Grundvåg, S.-A. and Mørk, A.: You learn as long as you drill; research synthesis from the Longyearbyen CO2 Laboratory, Svalbard, Norway, Nor. J. Geol., 99(2), 157–187, doi:10.17850/njg008, 2020.

Orvin, A. K.: Litt om kilder på Svalbard, Nor. Geol. Tidsskr. Norges Svalbard- og Ishavsundersøgelser, 10(57), 15–38, 1944.

835   van der Ploeg, M. J., Haldorsen, S., Leijnse, A. and Heim, M.: Subpermafrost groundwater systems: Dealing with virtual reality while having virtually no data, J. Hydrol., 475, 42–52, doi:10.1016/j.jhydrol.2012.08.046, 2012.

Pollock, D. W.: User Guide for MODPATH Version 7-A Particle-Tracking Model for MODFLOW, U.S. Geol. Surv. Open File Rep., 1086, 41, doi:10.3133/ofr20161086, 2016.

Riseborough, D., Shiklomanov, N., Etzelmüller, B., Gruber, S. and Marchenko, S.: Recent advances in permafrost modelling,
840   Permafr. Periglac. Process., 19(2), 137–156, doi:10.1002/ppp.615, 2008.

Robertson, E. C.: Thermal properties of rocks. Report 88-441, US Dep. Inter. Geol. Surv., 106, 1988.

Scheidegger, J. M. and Bense, V. F.: Impacts of glacially recharged groundwater flow systems on talik evolution, J. Geophys. Res. Earth Surf., 119(4), 758–778, doi:10.1002/2013JF002894, 2014.

Scheidegger, J. M., Bense, V. F. and Grasby, S. E.: Transient nature of Arctic spring systems driven by subglacial meltwater,
845   Geophys. Res. Lett., 39(12), 1–6, doi:10.1029/2012GL051445, 2012.

Schlumberger©: Petrel E&P, [online] Available from: https://www.software.slb.com/products/petrel, 2019.

Schuster, P. F., Schaefer, K. M., Aiken, G. R., Antweiler, R. C., Dewild, J. F., Gryziec, J. D., Gusmeroli, A., Hugelius, G., Jafarov, E., Krabbenhoft, D. P., Liu, L., Herman-Mercer, N., Mu, C., Roth, D. A., Schaefer, T., Striegl, R. G., Wickland, K. P. and Zhang, T.: Permafrost Stores a Globally Significant Amount of Mercury, Geophys. Res. Lett., 45(3), 1463–1471,
850   doi:10.1002/2017GL075571, 2018.

Singhal, B. B. S. and Gupta, R. P.: Applied Hydrogeology of Fractured Rocks, 2nd ed., Springer Netherlands., 2010.

Šuklje, L.: Rheologic Aspects of Soil Mechanics, 1st ed., Wiley-Interscience., 1969.

Svensson, H.: Pingos i yttre delen av Adventdalen, Nor. Polarinstitutt Årb. 1969, 168–174, 1970.

Taniguchi, M.: Evaluations of the saltwater-groundwater interface from borehole temperature in a coastal region, Geophys.

855   Res. Lett., 27(5), 713–716, doi:10.1029/1999GL002366, 2000.

Verruijt, A.: A note on the ghyben-herzberg formula, Int. Assoc. Sci. Hydrol. Bull., 13, 43–46, doi:10.1080/02626666809493624, 1968.

Walvoord, M. A. and Kurylyk, B. L.: Hydrologic impacts of thawing permafrost—a review, Vadose Zo. J., 15(6), doi:10.2136/vzj2016.01.0010, 2016.

860   Wangen, M., Souche, A. and Johansen, H.: A model for underpressure development in a glacial valley, an example from Adventdalen, Svalbard, Basin Res., 28(6), 752–769, doi:10.1111/bre.12130, 2016.

Williams, J. R.: Ground Water in the Permafrost Regions of Alaska, US Geol. Surv. Prof. Pap., 1970.

Williams, P. J. and Smith, M. W.: The ground thermal regime, in The Frozen Earth, pp. 83–121, Cambridge University Press., 1989.

865   Woo, M. K.: Permafrost Hydrology, Springer-Verlag Berlin Heidelberg., 2012.

Yoshikawa, K. and Harada, K.: Observations on nearshore pingo growth, Adventdalen, Spitsbergen, Permafr. Periglac. Process., 6(4), 361–372, doi:10.1002/ppp.3430060407, 1995.

Yoshikawa, K. and Nakamura, T.: Pingo growth ages in the delta area, Adventdalen, Spitsbergen, Polar Rec. (Gr. Brit)., doi:10.1017/S0032247400067565, 1996.

870